QUALIFICATION STRATEGIES FOR LASER PROCESSED INCONEL 718 USING ULTRASONIC NON-DESTRUCTIVE EVALUATION

By

Guillermo Eleazar Huanes Alvan

A DISSERTATION

Submitted to
Michigan State University
in partial fulfillment of the requirements
for the degree of

Mechanical Engineering—Doctor of Philosophy

2022

ABSTRACT

QUALIFICATION STRATEGIES FOR LASER PROCESSED INCONEL 718 USING ULTRASONIC NON-DESTRUCTIVE EVALUATION

By

Guillermo Eleazar Huanes Alvan

Laser-processed additive manufacturing (laser-AM) is a technology that allows the direct fabrication of metallic three-dimensional parts from a CAD model, with the particularity of using a laser as its energy source. The application of this technology to nickel-based superalloys (Ni-superalloys) attracts interest from the aircraft, aerospace, or power generation industry due to the outstanding strength at high temperatures and exceptional resistance to fatigue, hot corrosion, and wear under extreme conditions shown by these materials. However, the main drawbacks that prevent the implementation at a large scale of laser-AM nickel-based superalloys are the uncertainty of the mechanical integrity, quality and reproducibility of mechanical properties that can occur due to porosity, bonding defects, anisotropy, or heterogeneity present in the microstructure, which in turn is affected by the processing parameters. Furthermore, one of the principal aspects that prevents the adoption of this technology is the lack of a unified qualification standard that contemplates the needs of the aforementioned industries. Although several efforts are currently on track in the field of destructive testing for the characterization of AM materials in general, non-destructive techniques have merely been utilized for the detection of defects and their capability as a material characterization tool has not been deeply explored. In particular, ultrasonic non-destructive evaluation (ultrasonic NDE) stands out among other NDE techniques given its straightforward application and its sensitivity to microstructural variations that can be applied to complex materials such as Ni-superalloys fabricated with laser-AM technologies. The aim of this work is to show our efforts in the ultrasonic NDE characterization of as-fabricated Laser-Directed

Energy Deposition Inconel 718 (laser-DED IN718) and to derive parameters that can be further applied in a unified qualification standard for the acceptance of this material.

First, we present a baseline ultrasonic NDE comparison of Inconel 718 samples fabricated with Laser-Directed Energy Deposition and with hot-rolled to show their difference in ultrasonic velocities, ultrasonic attenuation, and ultrasonic backscattering and to further correlate the contributions of the laser-DED IN718 microstructure to these parameters. Then, utilizing the ultrasonic response of the hot-rolled sample and two laser-DED samples fabricated with different processing parameters, we derived for the first time ultrasonic NDE qualification parameters to quantify anisotropy, heterogeneity, grain, and grain clusters contributions to attenuation, and grain cluster sizes. Finally, we utilize ultrasonic NDE to characterize laser-DED multi-material structures of Inconel 718 and Stainless steel 420. The ultrasonic velocities, attenuation and backscatter coefficients responses are measured, and their values are compared to theoretical values derived from a simple rule of mixtures.

Dedicated to my loved ones.

ACKNOWLEDGMENTS

First and foremost I want to show my deepest gratitude to my advisor, Dr. Sunil Chakrapani, for his support, for his motivation making me appreciate the life of a researcher and for always being there as a mentor in research and life. My sincere gratitude to my dissertation committee Dr. Himanshu Sahasrabudhe, Dr. Firas Khasawneh and Dr. Prem Chahal for their guidance and for their encouraging words during my presentations. Also, I want to take the opportunity to thank Dr. Patrick Kwon, Dr. Katy Colbry and Dr. Mary-Anne Walker for their help ever since my first experience at MSU during my research internship in the summer of 2015. My special recognition to my professors during my undergraduate studies Dr. Jorge Olórtegui, Dr. José Olivencia and Dr. Víctor Alcántara for motivating me to pursue doctoral studies.

I thank my current and former labmates in the PUMA lab: Karthik, Aakash, Manoj, Mizan, Yoganandh, Subal, Alex and Zeb for their support and all the interesting conversations. Also, I want to thank my friends in the Mechanical engineering department: Aakash, Bibek, Archana, Beytullah, Tejas and Jiang for the good times we had in this adventure this past 4 years. Carolina, Omar, Pepe, Andrés, Melina, Martina, José H, and the rest of the group, thank you for making me feel home away from home. My Peruvian friends: Juanca, Lisi, Ana Paula, José, Romy, Ximena and Juan, thank you for your company either in person or virtually troughout these years.

I thank my parents Patricia and Ariel, my grandparents Juan, Olga, Eleazar and Ema, and the rest of my family for all their love and support and for always believing in me.

Last but not least, I thank Regina for being that special person who made everything seem better, for her love, her company, and for always reminding me of what I am capable of.

TABLE OF CONTENTS

LIST OF TABLES viii

LIST OF FIGURES ix

CHAPTER 1. INTRODUCTION 1

CHAPTER 2. ULTRASONIC CHARACTERIZATION OF STRUCTURES: MATERIALS AND METHODS 6
- 2.1. Samples 6
  - 2.1.1. IN718 6
  - 2.1.2. SS420-IN718 multi-material structures 7
- 2.2. Ultrasonic NDE methods 8
  - 2.2.1. Contact measurements 8
  - 2.2.2. Immersion measurements 11

CHAPTER 3. CHARACTERIZING THE AS-FABRICATED STATE OF ADDITIVELY FABRICATED IN718 USING ULTRASONIC NONDESTRUCTIVE EVALUATION 16
- 3.1. Elastic behavior 16
  - 3.1.1. Longitudinal Group velocity 16
  - 3.1.2. Shear velocity 17
  - 3.1.3. Elastic constants 18
- 3.2. Ultrasonic dispersion 19
- 3.3. Ultrasonic attenuation coefficient 20
- 3.4. Ultrasonic backscatter coefficient 21
- 3.5. Discussion 22
  - 3.5.1. Elastic behavior 26
  - 3.5.2. Ultrasonic attenuation coefficient 27
  - 3.5.3. Ultrasonic backscatter coefficient 28
- 3.6. Conclusions 29

CHAPTER 4. ULTRASONIC NDE QUALIFICATION PARAMETERS FOR IN718 DED STRUCTURES 31
- 4.1. Proposed qualification parameters 33
  - 4.1.1. Anisotropy index: A_{LS} 33
  - 4.1.2. Heterogeneity parameters: standard deviation (σ) and mean (μ) 34
  - 4.1.3. Attenuation coefficient parameters: A and B 36
  - 4.1.4. Ultrasonic scattering transition peaks: $P_{k\bar{d}=1}$ 36
- 4.2. Results 37
  - 4.2.1. Anisotropy index: A_{LS} 37

4.2.2. Heterogeneity parameters: standard deviation (σ) and mean (μ) 38
4.2.3. Attenuation coefficient parameters: A and B... 41
4.2.4. Ultrasonic scattering transition peaks: $P_{k\bar{d}=1}$ 42
4.3. Discussions.. 44
4.4. Conclusions 47

CHAPTER 5. ULTRASONIC CHARACTERIZATION OF SS420-IN718 MULTI-MATERIAL STRUCTURES FABRICATED USING LASER DIRECTED ENERGY DEPOSITION 48
5.1. SS420-IN718 multi-material structures 50
5.2. Experimental details of ultrasonic testing 51
5.2.1. Ultrasonic velocities.. 51
5.2.2. Ultrasonic attenuation coefficient 51
5.2.3. Ultrasonic backscatter coefficient... 53
5.3. Rule of mixtures (RoM) 54
5.4. Results 56
5.4.1. Ultrasonic velocities.. 56
5.4.2. Attenuation coefficient... 57
5.4.3. Backscatter coefficient... 58
5.4.4. Elastic constants.. 59
5.5. Discussions.. 60
5.5.1. Elastic properties... 61
5.5.2. Attenuation coefficient... 63
5.5.3. Backscatter coefficient... 64
5.5.4. Rule of mixture 65
5.5.5. Heterogeneity.. 66
5.6. Conclusions 67

CHAPTER 6. CONCLUSIONS AND FUTURE WORK.. 69

REFERENCES 71

LIST OF TABLES

Table 2.1. Phases observed in IN718 [26]. 6

Table 3.1. Longitudinal group velocity of IN718 DED and hot-rolled. 17

Table 3.2. Elastic constants of the IN718 DED and hot-rolled samples...................................... 19

Table 4.1. Percentage difference between A_{LS} of samples and $A_{LS} = 1$. 38

Table 4.2. Scattering transition frequencies and corresponding average cluster size.................. 43

Table 5.1. Mixed samples densities measured with the Archimedes method. 50

Table 5.2. Theoretical mechanical properties [74,75]. 55

Table 5.3. Elastic constants measured from the ultrasonic velocities... 59

Table 5.4. Mechanical properties of the sample [12]... 60

LIST OF FIGURES

Figure 1.1. Relation between laser-AM processing parameters and ultrasonic NDE characterization parameters. 4

Figure 2.1. (a) Laser-DED sample fabrication setup, (b) 1-inch cube sample. 7

Figure 2.2. Schematic showing sample fabrication. Dual feeders are used to feed two different powders. 8

Figure 2.3. (a) Contact-based setup for ultrasonic velocity measurements, (b) shear transducer polarization. 9

Figure 2.4. Relationship between ultrasonic velocities (V_{ij}) and elastic constants (C_{ij}).......... 10

Figure 2.5. MATLAB plot of a longitudinal waveform and its Hilbert transform envelope used for ultrasonic group velocity calculation. 11

Figure 2.6. Immersion-based broadband setup used to measure attenuation coefficient and backscatter coefficient of IN718 samples. 12

Figure 3.1. Longitudinal group velocity as function of frequency of IN718: (a) DED and (b) hot-rolled samples. 17

Figure 3.2. Shear velocity of IN718: (a) DED and (b) hot-rolled samples. 18

Figure 3.3. Elastic constants of the IN718 DED and hot-rolled samples. 19

Figure 3.4. Phase velocity comparison between hot-rolled and laser-DED samples. 20

Figure 3.5. Ultrasonic attenuation coefficient of a hot-rolled IN718 sample. 20

Figure 3.6. Attenuation coefficient (a, b, c) of IN718 DED sample in its three directions measured with a 5 MHz planar transducer. 21

Figure 3.7. Backscatter coefficient of IN718 hot-rolled at 15 MHz. 22

Figure 3.8. Backscatter coefficient (a, b, c) of IN718 DED sample in its three directions measured with a 10 MHz F=4in transducer focused at mid-plane. 22

Figure 3.9. SEM image of IN718 hot-rolled sample along its rolling direction [12]. 23

Figure 3.10. Micrographs of the IN718 laser-DED sample showing the build direction. Scale: 500 microns [12]. 24

Figure 3.11. Micrographs of the IN718 laser-DED sample showing the XY plane. Scale: 500 microns [12]. 25

Figure 3.12. Micrographs of the IN718 laser-DED sample showing the XY plane. Scale: 100 microns [12]. 25

Figure 3.13. (a) macrograin and (b) micrograin relation to the Rayleigh-stochastic scattering transition frequency. 26

Figure 3.14. B-scan of shear wave birefringence (a, b, c) of the IN718 DED sample. 27

Figure 4.1. Process to obtain the standard deviation (σ) and mean (μ) qualifying parameters from a back-wall amplitude C-Scan. 35

Figure 4.2. Anisotropy index of the laser-DED samples PP1 and PP2 compared to a hot-rolled sample. 38

Figure 4.3. Grayscale backwall amplitude C-Scans and their corresponding pixel counts and Gaussian distribution plotted against energy loss represented in decibels. 39

Figure 4.4. Heterogeneity parameters σ (a) and μ (b) of the PP1, PP2 and hot-rolled samples... 40

Figure 4.5. Ultrasonic attenuation coefficient and the corresponding attenuation model fitted for the samples PP1, PP2 and hot-rolled. 41

Figure 4.6. Attenuation model $\alpha(f_{MHz}) = Af^4 + Bf^2$ fitting parameters A (a) and B (b). 42

Figure 4.7. Average cluster size of the PP1 and PP2 samples as a function of the frequencies where the peaks appeared. 43

Figure 4.8. Identified qualification parameters and their metrics obtained from ultrasonic NDE characterization. 45

Figure 5.1. A-Scan showing the multiple echoes from the samples after immersed in water; (a) 100% SS420, and (b) 25% IN718. The backscattered amplitudes and the region chosen for processing the backscatter coefficient for (c) 100% SS420, and (d) 25% IN718. To show the relative backscattered amplitudes, the backwall is also shown. (e) A-Scan showing the reference echo to capture the transducer response, and (f) spectral response of the reference echo which was used for the backscatter coefficient determination. 52

Figure 5.2. (a) Longitudinal velocity along three directions, (b) Shear wave velocity along different shearing planes (Di–j), i is the propagation direction and j is the shear direction. RoM corresponds to the rule of mixture assuming the sample to be isotropic. 56

Figure 5.3. Attenuation coefficient as a function of frequency for (a) 100% SS420, (b) 25% IN718, (c) 50% IN718, (d) 75% IN718 and (e) 100% IN718. 57

Figure 5.4. Backscatter coefficient as a function of frequency for (a) 100% SS420, (b) 25% IN718, (c) 50% IN718, (d) 75% IN718 and (e) 100% IN718. 58

Figure 5.5. Micrographs of (a) 100% SS420, (b) 25% IN718, (c) 50% IN718, (d) 75% IN718 and (e) 100% IN718. The vertical direction is the build direction (z-axis). The images are sections of the XZ, YZ planes [12]. 61

Figure 5.6. XRD analysis showing different phases for (a) 100% SS420, (b) 25% IN718, (c) 50% IN718, (d) 75% IN718 and (e) 100% IN718 [12]. 62

Figure 5.7. Spatial C-Scan of the 25% IN718 sample for (a) backwall amplitude (BW), (b) Backscatter RMS calculated in the frequency domain. 67

CHAPTER 1. INTRODUCTION

Laser-processed additive manufacturing (laser-AM) comprises several technologies that allow the fabrication of three-dimensional structures from a CAD model in a layer-by-layer fashion, in contrast with conventional manufacturing where subtraction of material is predominant. Laser-AM has shown progress in the fabrication of complex metallic materials such as nickel-based superalloys [12-20], which are within the most important engineering materials due to their superior mechanical properties and behavior under high-temperature conditions, characteristics that make them ideal for application in the aerospace or power generation industry [12-15]. The eventual adoption of these laser-AM parts on a large scale appears promising. However, one of the principal challenges that AM faces is the ability to produce complex components that can respond with high reliability in critical services. For these reasons, qualification, certification, and product acceptance are important affairs in AM industry that are not yet in their final stage.

The Federal Aviation Administration (FAA) was one of the first institutions in approving the use of an AM part for an engine of commercial jets [1,3]. It was this event that originated the first standard approved by ASTM and ISO [1]. Nowadays, there are over a dozen standards that address several aspects of AM, such as terminology, design, materials and processes, and test methods [1-11]. However, there is still progress in developing and expanding the scope of new standards from different agencies around the globe [1]. Part certification and qualification appears to be more challenging since several factors could affect the reproducibility of products, such as feedstock material, the chosen laser-AM technology and post-processing of the as-fabricated product [6-11].

Laser Directed Energy Deposition (laser-DED) is among the laser-AM technologies, and it consists of several processing parameters including laser power, scan speed, hatch spacing, layer thickness, particle shape/size distribution and other build conditions. A wrongful choice of these parameters can result in parts with internal defects such as porosity or lack of fusion [6-11]. This becomes particularly important in the fabrication of nickel-based superalloys, where the multiple melting and solidification during fabrication, inherent of any laser-AM technology, result in complex polycrystalline microstructures composed of grains of a wide distribution of sizes, shapes, and orientations. They are considered statistically isotropic when the grains are randomly oriented; however, this rarely happens, especially with parts fabricated with laser-AM technologies where the cooling rates have a direct effect on grain morphology [12-20]. The as-fabricated parts will exhibit texture or a preferred orientation of grains that will result in anisotropic properties of the part with the build direction being different than the transverse directions. This and other mechanical behavior such as strength, fatigue, hardness, or residual stress have been studied using destructive methods, where the influence of the processing parameters on these mechanical properties can be observed and attributed for example to the presence of porosity, lack of fusion, flaws, etc. [12-20,23]. At the same time, ASTM and ISO are advancing in their effort to establish a unified standard for several types of AM technologies, including laser-DED and more specifically, with nickel-based superalloys as described by the standards F3055-14a and F3056-14 for Inconel 718 and Inconel 625, respectively [40,41]. Although this progress does not close the gap in the case of materials with complex microstructure that can present anisotropy, microstructural heterogeneity or even the presence of cluster of grains having different sizes.

However, non-destructive (NDE) techniques have not been deeply explored, NDE plays an important role in the inspection of components since it comprises a set of techniques that allow the detection of defects or the quantification of mechanical properties [21-23]. The range of application of NDE methods depend on the dimensions of the feature to be inspected or its depth in the component. Ultrasonic evaluation is the NDE technique with more implementation feasibility from all NDE methods, its major advantage is the depths it could inspect. This technique can also be used to obtain 2D images at different depths of a surface when using a focused transducer. This allows inspection of any depth without compromising the resolution of the image. This image not only contains location of defects, but it can also be used to quantify the mechanical properties such as stiffness as function of position, or also to determine the variation of the quality of the AM part. What makes ultrasonic NDE more attractive is that it can be used not only for defect detection but, more importantly, for material characterization. Ultrasonic NDE has been extensively used for the study of polycrystalline materials [28-30]. However, most of these studies have focused on defect detection or porosity quantification. Small progress has been achieved regarding the study of AM nickel-based superalloys where, for instance, ultrasonic velocities have been used to quantify the anisotropy of the parts fabricated with laser-AM techniques [23]. There is still a great deal of work ahead in order to understand and correlate processing parameters to microstructure, which in turn mandates the mechanical behavior of the parts. As it was mentioned earlier in this paragraph, there is a strong connection between laser-AM processing parameters and microstructure, and ultrasonic NDE parameters are sensitive to microstructural features, therefore, evaluating the ultrasonic response of laser-AM parts with quantifiable parameters will lay the foundations for developing an ultrasonics non-destructive qualification framework for laser-AM nickel-based superalloys and will also contribute to the optimization of their processing parameters and eventual adoption of laser- AM technologies in more industries.

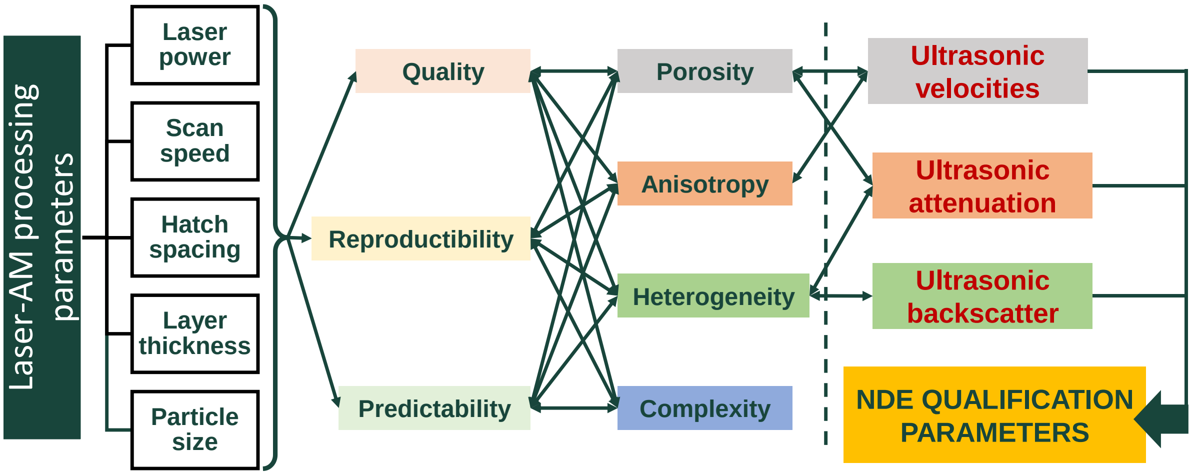

Figure 1.1. Relation between laser-AM processing parameters and ultrasonic NDE characterization parameters.

This work is divided in three main ideas where we used ultrasonic NDE for the characterization of laser-DED materials. First, in chapter 2, the materials and ultrasonic method used in this thesis are presented. The correlation between ultrasonic velocity and elastic behavior is described. Also, the ultrasonic frequency dependent parameters: ultrasonic attenuation and ultrasonic backscattering are detailed and their relationship to grain size is explained.

Chapter 3 presents the material characterization of the laser-DED as-fabricated nickel superalloy Inconel 718 (IN718) realized with ultrasonic evaluation. The ultrasonic velocities, attenuation and backscatter coefficients were chosen as material characterization parameters given their sensitivity to microstructural features. Ultrasonic velocities are connected to the elastic behavior of the materials and can be used to quantify their elastic anisotropy; we also explored material dispersion by studying the variation of ultrasonic velocities with the variation of the frequency of the ultrasonic wave. The attenuation and backscattering coefficients are frequency dependent parameters, the former quantifies the overall loss of energy of an ultrasonic wave after it traveled through a medium and the latter quantifies the contribution of the internal grains or defects to the backscattered ultrasonic wave energy. The ultrasonic response of the laser-DED

IN718 is compared to that of a hot-rolled IN718 sample, since hot-rolling is a widely accepted conventional fabrication method and because rolled samples could have elongated grains that can influence its ultrasonic response [24-25], similarly as with the columnar dendritic grains present in laser-DED samples [12-20,26].

In chapter 4, and by using the ultrasonic parameters obtained in chapter 3, ultrasonic qualification parameters are derived in order to characterize the inherent characteristics of laser-DED IN718 materials such as anisotropy, microstructural heterogeneity and size of cluster of grains. These qualification parameters are compared between two samples fabricated with different laser-power and scan speed. Furthermore, they are also compared to a hot-rolled sample with neglected anisotropy, heterogeneity and without the presence of clusters of grains.

Lastly in chapter 5, five multi-material structures varying from 100% stainless steel 420 to 100% Inconel 718 are characterized with ultrasonic NDE with the three main parameters: velocity, attenuation, and backscattering. The samples showed different degrees of anisotropy and the variation of ultrasonic parameters was not linear as exhibited by a simple rule of mixtures derived from theoretical values. It was observed that the presence of Inconel 718 contributed greatly to the microstructural heterogeneity of the mixed samples.

CHAPTER 2. ULTRASONIC CHARACTERIZATION OF STRUCTURES: MATERIALS AND METHODS

2.1. Samples

2.1.1. IN718

Our collaborators at the Laboratory of Advanced Manufacturing at Michigan State University fabricated an IN718 cube using a laser-DED machine. IN718 is a multiphase nickel superalloy with composed of 50 – 55 wt% of Ni, 17 – 21 wt% of Cr, 4.8 – 5.5 wt% of Nb, 2.8 – 3 wt% of Mo, 0.65 – 1.15 wt% of Ti, 1 wt% of Co and small amount of Al and Fe [14]. These elements formed several phases, as shown in Table 2.1 [26].

Phase	Crystal structure	Chemical formula
$\boldsymbol{\gamma}$	fcc	Ni
$\boldsymbol{\gamma''}$	bct (ordered $D0_{22}$)	Ni_3Nb
$\boldsymbol{\gamma'}$	fcc (ordered $L1_2$)	$Ni_3(Al,Ti)$
$\boldsymbol{\delta}$	orthorhombic (ordered $D0_a$)	Ni_3Nb
MC	cubic B_1	(Nb,Ti)C
Laves	hexagonal C_{14}	$(Ni,Fe,Cr)_2(Nb,Mo,Ti)$

Table 2.1. Phases observed in IN718 [26].

The fabrication was carried out in argon environment with the oxygen and moisture levels below 20 ppm. The IN718 powder particle size was distributed between 44 – 106 µm were utilized. The laser power varied from 900 – 1000W. The approximate nozzle travel speed was between 20 to 22 mm/sec. Fig. 2.1 (a) shows a schematic diagram of the laser-DED process. The sample was deposited as 1-inch cube on a 12 mm thick stainless steel 304 (SS304) base plate, as shown in Fig. 2.1 (b). It was further cut from the base plate and machined to a final dimension of 25 mm X 25 mm X 23 mm, the latter being the build direction (Z-direction) thickness. The sample surface was equivalent to 400 grit surface finish. The density of the sample was measured using the Archimedes method which resulted in a density of 8237 kg/m^3. To compare the results from the laser-DED sample to a conventionally manufactured sample, a hot-rolled IN718 alloy sample of 18 mm X 17 mm X 26 mm was used.

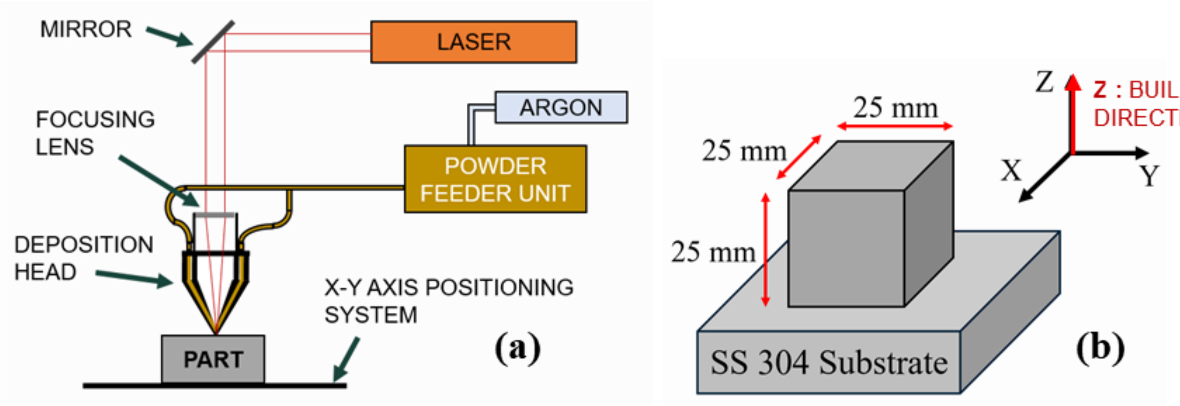

Figure 2.1. (a) Laser-DED sample fabrication setup, (b) 1-inch cube sample.

2.1.2. SS420-IN718 multi-material structures

Multi-material structures were fabricated using a Laser Engineered Net Shaping (LENS) rapid Laser DED machine at Optomec Inc. (NM, USA). Schematic diagram of the Laser DED process is shown in Fig. 2.2. The fabrication was carried out in argon environment with the oxygen and moisture levels below 20 ppm. Stainless steel 420 (SS420) and Inconel 718 (IN718) powders with particle size distribution between 44 – 106 µm (Carpenter Powder Products, PA, USA) were utilized. A YLS 1000 laser (IPG Photonics - MA, USA) with power varying from 900 – 1000W was used to fabricate the samples. Approximate deposition speed was 15 to 17 mm/sec. Two powder feeder modules carrying SS420 and IN718 were used to feed the mixed powders onto the substrate. By calibrating the powder feeders to establish the feeder motor speed (RPM) and powder mass feed-rate (g/min), we were able to change the weight ratio of each alloy in the mixture. Using this calibration, samples were fabricated with five different compositions (by weight): (a) 100% SS420, (b) 75% SS420 – 25% IN718, (c) 50% SS420 – 50% IN718, (d) 75% IN718 – 25% SS420 and (e) 100% IN718. The samples were deposited as 25 mm cubes on a 12 mm thick stainless steel 304 base plate. The samples were further cut from the base plates and machined to a final dimension of 25 mm (L) X 25 mm (W) X 19 mm (H) samples, the latter being the build direction thickness. The final surface finish was equivalent to a 400-grit surface finish.

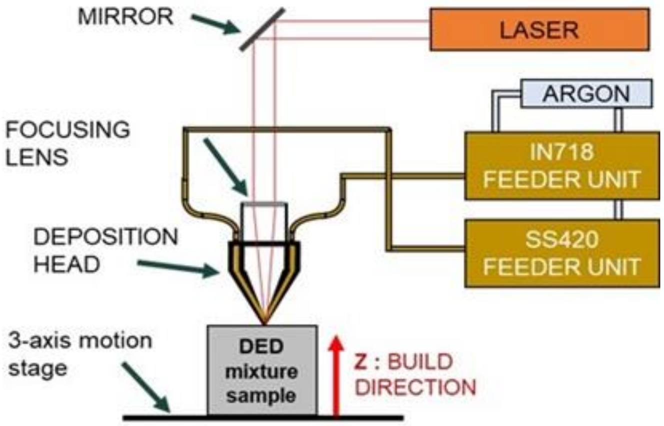

Figure 2.2. Schematic showing sample fabrication. Dual feeders are used to feed two different powders.

2.2. Ultrasonic NDE methods

The two experimental methods used, contact and immersion, and the ultrasonic parameters measured are explained in the following subsections.

2.2.1. Contact measurements

The experimental setup consists of a pulser/receiver that sends a broadband spike input to a narrow band piezoelectric contact transducer which then converts it into elastic waves that propagate through the sample. Fig. 2.3 (a) shows the setup that was used for the contact-based experiments to measure the group and phase velocities of the longitudinal and shear waves.

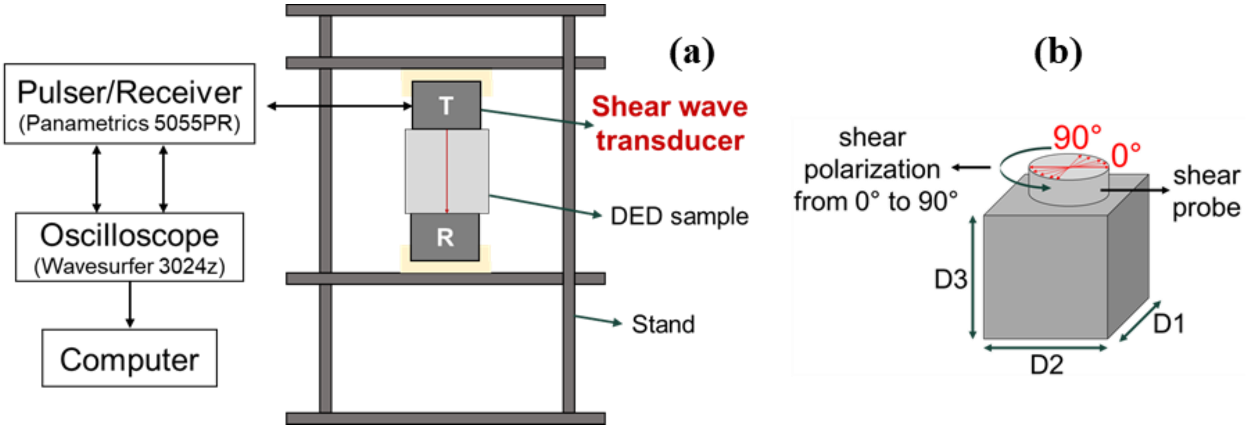

Figure 2.3. (a) Contact-based setup for ultrasonic velocity measurements, (b) shear transducer polarization.

The elastic constants of a solid material can be calculated from the longitudinal (V_L) and shear (V_S) ultrasonic velocities. The relationship between these sound velocities and the modulus of elasticity (E_L), Poisson's ratio (ν) and density (ρ) are expressed as follows:

$$V_L = \sqrt{\frac{E_L(1-\nu)}{\rho(1+\nu)(1-2\nu)}} \ldots \text{(Eq. 2.1)}$$

$$V_S = \sqrt{\frac{E_L}{2\rho(1+\nu)}} \ldots \text{(Eq. 2.2)}$$

Every metallic material is elastically anisotropic (in different degrees). In a more general way, an anisotropic material is described using its elastic constants (C_{ij}) that are represented with the stiffness matrix. This describes the crystallographic symmetry of the structure, and its values can be used to quantify the degree of anisotropy of the material. Ultrasonic longitudinal and shear velocities propagation along the principal axes of the structure can be used to obtain the principal diagonal of the stiffness matrix as shown in Fig. 2.4.

The group velocity measurements were conducted using a 5, 10 and 15 MHz contact transducers for longitudinal waves and at 2.25 MHz for shear waves. The longitudinal phase velocity of the hot-rolled and laser-DED cube samples was measured with a 1 MHz transducer.

Shear waves are more sensitive to elastic anisotropy than longitudinal waves. Fig. 2.3 (b) shows a shear wave transducer, with its fixed polarization direction (or particle motion direction), being rotated about the Z (D3 or build direction) axis from 0 to $\pi/2$ with steps of $\pi/12$ to measure the shear velocity of the sample at different polarization angles and therefore compare the anisotropy of the laser-DED sample to the hot-rolled sample. All the ultrasonic velocities were measured in the three propagation directions: D1, D2 and D3, the latter being the laser-DED sample build direction.

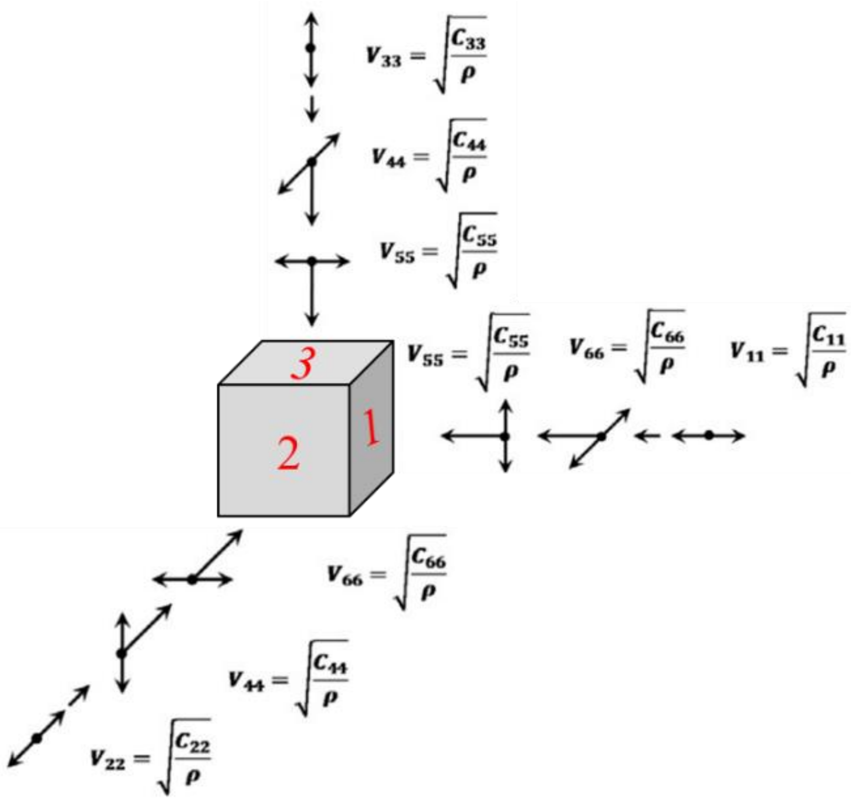

Figure 2.4. Relationship between ultrasonic velocities (V_{ij}) and elastic constants (C_{ij}).

The longitudinal velocities were measured in pulse-echo mode where the transducer acts as the transmitter and the receiver. The wave travels two times the thickness of the sample or from the front-wall to the back-wall (top to bottom) and the echoes collected correspond to each reflection from the back-wall. The shear velocities were measured in through-transmission mode, as seen in Fig. 2.3 (a), where the transmitter and receiver were positioned at the front-wall and the back-wall of the sample, respectively, and the wave travels once through the thickness of the sample. The collected waveforms (digitized at 1GHz using an 8-bit oscilloscope) were processed in MATLAB to obtain the ultrasonic group velocities by dividing the propagation path (thickness of the sample) by the time difference of the peaks of the envelope of a Hilbert transform applied to the waveform, these peaks represent the first and second reflections from the back-wall. Fig. 2.5 shows a typical time-dependent ultrasonic signal (A-scan) or waveform for longitudinal sound wave propagation along one direction of the IN718 DED 1-inch cube and the equation used for determining the longitudinal velocity in pulse-echo mode.

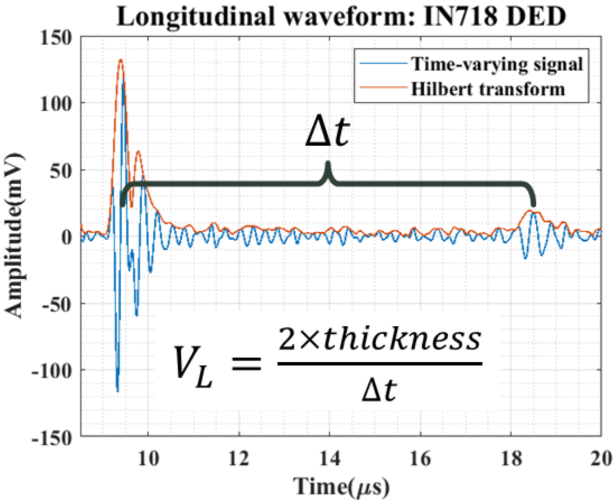

Figure 2.5. MATLAB plot of a longitudinal waveform and its Hilbert transform envelope used for ultrasonic group velocity calculation.

2.2.2. Immersion measurements

Similarly, as the contact-based experiments, a pulser/receiver was used to send a broadband spike to the immersion transducer. The experiments were conducted in pulse-echo mode. The samples were immersed in water and the immersion transducer was normalized to the sample surface. Then, an ultrasonic wave coming from the transducer traveled through water before being transmitted to the sample. An A-scan containing the echoes from the front-wall and back-wall reflections and the noise between these echoes were collected from each of the positions the transducer moved. Fig. 2.6 shows a typical immersion setup, x_w and x_s are the water-path and thickness of the sample, respectively; A, B and C correspond to the front-wall, first back-wall and second back-wall echo amplitudes when they reach the transducer after they traveled through the water and sample. Both the ultrasonic attenuation and ultrasonic backscattering coefficients were measured with this method.

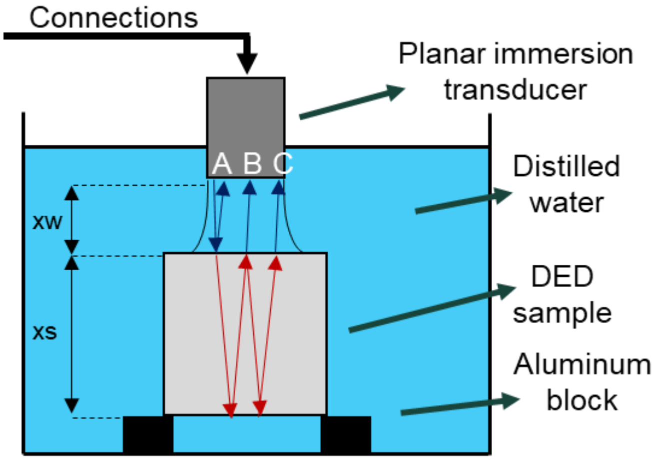

Figure 2.6. Immersion-based broadband setup used to measure attenuation coefficient and backscatter coefficient of IN718 samples.

For the attenuation measurement, echoes A and B were individually collected as A-scans and then processed. The planar ultrasonic immersion transducer is placed at a position where its face is in contact with water and the transducer is aligned with the center of the sample; then the transducer sends an ultrasonic wave that travels through water, when the wave reaches the interface water-specimen, part of the acoustic energy is reflected back to the transducer as echo A (front-wall) and part of the energy is transmitted to the specimen, this transmitted wave reaches the bottom of the specimen and reflects from the interface sample-water, it travels back transmitting again through the top of the specimen and then reaching the transducer as echo B (first back-wall). The amplitude of each echo is expressed as it follows:

A = $\boldsymbol{FW} = A_0 * e^{-2\alpha_w x_w} * R_{ws} * D(s_{FW})$ … (Eq. 2.3)

B = $\boldsymbol{BW1} = A_0 * e^{-2\alpha_w x_w} * T_{ws} * R_{sw} * T_{sw} * e^{-2\alpha_s x_s} * D(s_{BW1})$ … (Eq. 2.4)

Where:

- $\boldsymbol{FW}$ and $\boldsymbol{BW1}$ are the amplitudes of the front-wall and first back-wall echoes.
- $\boldsymbol{A_0}$ is the initial amplitude of the wave coming from the transducer.
- $\boldsymbol{\alpha_w}$ and $\boldsymbol{\alpha_s}$ are the attenuation coefficients of the water and the sample, respectively.
- $\boldsymbol{x_w}$ and $\boldsymbol{x_s}$ are the water path and the thickness of the specimen, respectively.
- $\boldsymbol{R_{ws}}$, $\boldsymbol{R_{sw}}$, $\boldsymbol{T_{ws}}$, $\boldsymbol{T_{sw}}$ are the reflection and transmission coefficients at the interface water-sample and sample-water.
- $\boldsymbol{D(s_{FW})}$, $\boldsymbol{D(s_{BW1})}$, are the Lommel-Diffraction corrections [27]:

$$D(s) = 1 - e^{-(\frac{2\pi i}{s})}\left[J_0\left({}^{2\pi}/_{s}\right) + iJ_1\left({}^{2\pi}/_{s}\right)\right] \text{ … (Eq. 2.5)}$$

$$s = {}^{4\pi z}/_{ka^2} \text{ … (Eq. 2.6)}$$

  - z is the propagation distance.
  - a is the transducer radius.
  - k is the wavenumber, $k = \frac{\omega}{c} = \frac{2\pi f}{c}$, where f is the frequency and c the ultrasonic velocity.

Finally, taking the amplitude ratio between the consecutive echoes, the attenuation coefficient of the sample is determined as:

$$\boldsymbol{\alpha_s} = \frac{\mathbf{1}}{\mathbf{2}\boldsymbol{x_s}} \boldsymbol{ln}\left(\left|\frac{\boldsymbol{FW(f)}}{\boldsymbol{BW1(f)}}\right| * (\boldsymbol{R_{sw}}^{\mathbf{2}} - \mathbf{1}) * \left|\frac{\boldsymbol{D(s_{BW1})}}{\boldsymbol{D(s_{FW})}}\right|\right) \ldots \text{(Eq. 2.7)}$$

The backscattering coefficient was obtained after processing a collected C-scan, i.e., a 10 mm X 10 mm area of the sample is scanned and for each position where the focused immersion transducer moves, an A-scan is collected. The time-domain region of interest is between the front-wall and first back-wall echoes since within this region, the loss of wave energy due to scattering occurs. All the processing is performed in the frequency-domain. The ultrasonic backscattering coefficient is calculated as:

$$\sqrt{\boldsymbol{\eta}} = \frac{|\boldsymbol{\Gamma_{sample}}(\boldsymbol{f})|\,|R_{w-ref}|\,a^2\rho_w v_w\,|D_{ref}|k_s}{|\Gamma_{ref}(f)|\,2{T_{ws}}^2\rho_s v_s e^{2\alpha_w x_w}}\;\frac{1}{\left[\iiint_{-\infty}^{\infty}|C(f,x_1,y_1,z_1)|^4\,P(z_1)e^{-4\alpha_s z_s}\,dx_1dy_1dz_1\right]^{1/2}} \ldots \text{(Eq. 2.8)}$$

Where:

- $\boldsymbol{\eta}$ is the backscatter coefficient as a function of frequency.
- $|\boldsymbol{\Gamma_{sample}}(\boldsymbol{f})|$ is the backscatter spatial RMS magnitude of the sample in frequency domain.

$$|\boldsymbol{\Gamma_{sample}}(\boldsymbol{f})| = \sqrt{\frac{\sum_{i=1}^{n}|\boldsymbol{\Gamma_i}(\boldsymbol{f})|^2}{\boldsymbol{n}}} \ldots \text{(Eq. 2.9)}$$

Where $|\Gamma_i(f)|$ is the FFT of the windowed backscatter region in time-domain for the scan position "i" of the sample and "n" is the number of scan positions of the sample.

- $|\boldsymbol{\Gamma_{ref}}(\boldsymbol{f})|$ is the reference echo magnitude in frequency domain, this corresponds to the front-wall echo of the sample.
- $\boldsymbol{D_{ref}}$ is the diffraction correction for the front-wall reference echo.
- $\boldsymbol{R_{ws}}$ is the reflection coefficient between water and the sample.
- $\boldsymbol{T_{ws}}$ is the transmission coefficient between water and the sample.
- $\boldsymbol{k_s}$ is the wavenumber of the sample.

- $\boldsymbol{a}$ is the transducer radius.
- $\boldsymbol{\rho_w}$, $\boldsymbol{\rho_s}$ are the densities of the water and the sample, respectively.
- $\boldsymbol{v_w}$, $\boldsymbol{v_s}$ are the longitudinal velocities of the water and the sample, respectively.
- $\boldsymbol{\alpha_w}$, $\boldsymbol{\alpha_s}$ are the attenuation coefficients of the water and the sample, respectively.
- $\boldsymbol{C(f, x_1, y_1, z_1)}$ beam focal properties.
- $\boldsymbol{P(z_1)}$ corrects for time-domain window interval (equal to 1 within the interval and 0 outside of the interval).

The integral $\left[\iiint_{-\infty}^{\infty} |C(f, x_1, y_1, z_1)|^4 \, P(z_1) e^{-4\alpha_s z_s} \, dx_1 dy_1 dz_1\right]$ is used to compensate for the transducer focusing properties.

CHAPTER 3. CHARACTERIZING THE AS-FABRICATED STATE OF ADDITIVELY FABRICATED IN718 USING ULTRASONIC NONDESTRUCTIVE EVALUATION

This chapter deals with the baseline comparison of IN718 DED and hot-rolled structures with ultrasonic techniques. These two materials exhibit differences in their elastic behavior as it is shown with the ultrasonic velocities, which in turn can be owed to the difference in microstructural features (grain size, grain orientation, phases). Moreover, a dependence of the ultrasonic longitudinal velocity with the increase of transducer frequency is observed which open the door for an evaluation of the ultrasonic frequency-dependent properties, i.e., the attenuation coefficient and the backscatter coefficient. These properties, as explained earlier in this document, are extremely dependent of the grain size which act as scatterers of the wave energy, results of this parameters of the DED and hot-rolled samples are presented.

3.1. Elastic behavior

3.1.1. Longitudinal Group velocity

As explained before, this experiment was conducted using transducers of 5, 10 and 15 MHz to observe a possible dependence of the velocity with frequency. Fig. 3.1 shows the longitudinal group velocity of the DED (a), and hot-rolled (b) samples, the values are summarized in Table 3.1.

It can be observed a quasi-isotropic behavior and negligible variation with frequency in the hot-rolled sample. The maximum variation in velocity is 1.00% between D1 and D3. The increase in frequency causes a reduction in velocity of 0.66% in D1 between 5 and 15 MHz. The longitudinal velocity of the DED sample shows a greater dependence of propagation direction. The variation between D1 and D3 (build direction) is of 4.41%. The reduction of the velocity due to increase in frequency along D1 is of 1.32% and in the build direction is 1.00%. Although low, it still shows a greater variation with frequency than the hot-rolled sample. The reduction of velocity as the frequency increases happens because of ultrasonic wave dispersion. To understand this phenomenon better, the ultrasonic velocity dispersion (ultrasonic phase velocity) was studied, and the results are shown in Ch. 3.2.

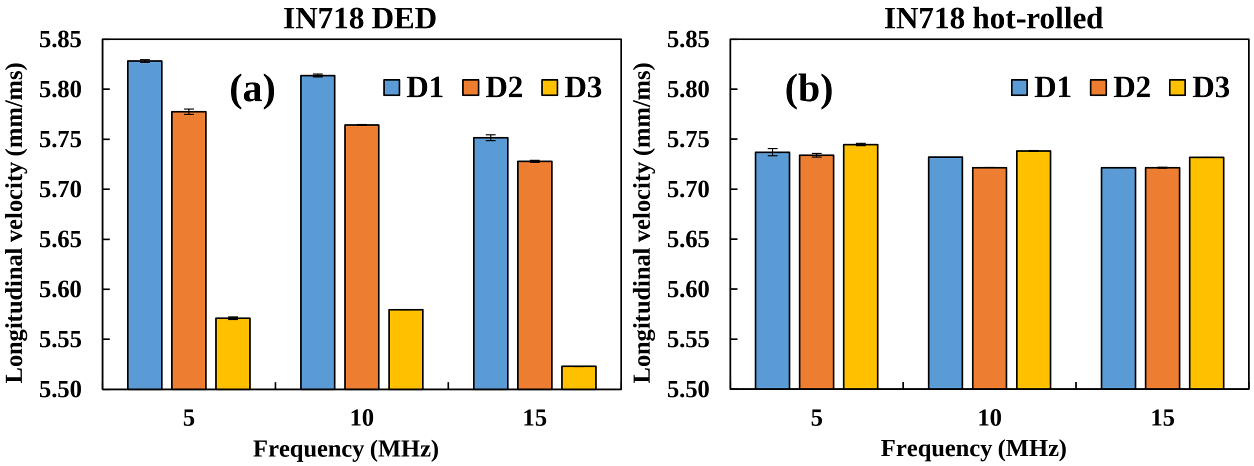

Figure 3.1. Longitudinal group velocity as function of frequency of IN718: (a) DED and (b) hot-rolled samples.

Freq (MHz)	**IN718 DED**			**IN718 hot-rolled**		
	D1	**D2**	**D3**	**D1**	**D2**	**D3**
5	5828.31 ± 1.33	5777.48 ± 2.58	5571.06 ± 1.22	5736.85 ± 3.60	5733.97 ± 1.88	5744.61 ± 1.24
10	5813.74 ± 1.35	5764.34 ± 0.45	5579.50 ± 0.04	5731.99 ± 0.01	5721.49 ± 0.19	5738.24 ± 0.47
15	5751.47 ± 2.90	5727.89 ± 0.95	5523.04 ± 0.01	5721.32 ± 0.09	5721.44 ± 0.61	5731.89 ± 0.06

Table 3.1. Longitudinal group velocity of IN718 DED and hot-rolled.

3.1.2. Shear velocity

The shear velocity was measured following the procedure described in Ch. 2.2.1 in through-transmission. Fig. 3.2 shows shear velocities of the IN718 samples. It can be observed how for the hot-rolled sample the velocity remains constant as the polarization angle varies, on the other hand, the laser-DED sample exhibits a greater degree of elastic anisotropy where, for the transverse directions D1 and D2, the velocity increases when the polarization direction is D3 (build direction). The difference between the velocities at 0° and 90° for D1 and D2 are ~22% whereas for the build direction (D3) the variation is only of 1.28%.

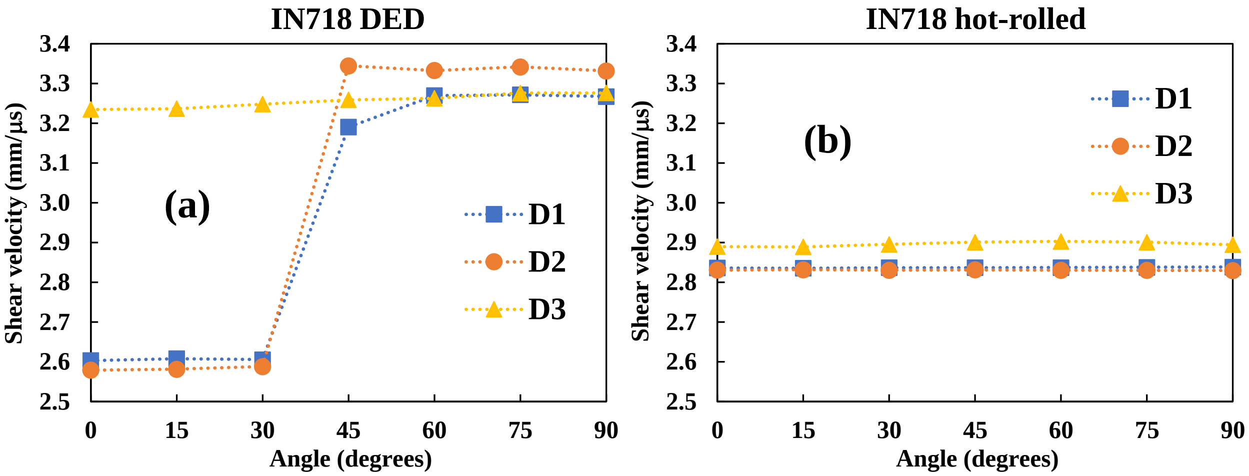

Figure 3.2. Shear velocity of IN718: (a) DED and (b) hot-rolled samples.

3.1.3. Elastic constants

Using the longitudinal and shear group velocities at 5 and 2.25 MHz, respectively, and with the equations shown in Fig. 2.4, the elastic constants were calculated and are shown in Fig. 3.3 and their values in Table 3.2. The density of the DED sample was measured to be 8237 kg/m^3 and for the hot-rolled, the theoretical density value of 8190 kg/m^3 was used.

The hot-rolled sample can be considered as isotropic or as having cubic symmetry since $C_{11} \approx C_{22} \approx C_{33}$ and $C_{44} \approx C_{55} \approx C_{66}$. For the DED sample $C_{11} \neq C_{22} \neq C_{33}$ and $C_{44} \approx C_{55}, C_{66}$. These results indicate that the studied DED sample is anisotropic, and its stiffness matrix possibly has orthorhombic symmetry.

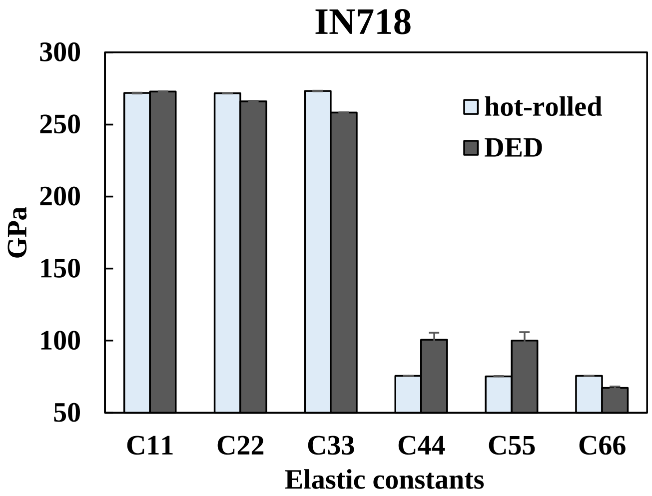

Figure 3.3. Elastic constants of the IN718 DED and hot-rolled samples.

C_{ij} (GPa)	IN718 DED	IN718 hot-rolled
C_{11}	272.78 ± 0.33	271.84 ± 0.34
C_{22}	266.01 ± 0.44	271.74 ± 0.14
C_{33}	258.28 ± 0.26	273.21 ± 0.22
C_{44}	100.64 ± 4.83	75.58 ± 0.05
C_{55}	100.01 ± 5.90	75.26 ± 0.07
C_{66}	67.29 ± 0.92	75.52 ± 0.12

Table 3.2. Elastic constants of the IN718 DED and hot-rolled samples.

3.2. Ultrasonic dispersion

When the ultrasonic velocity changes as the frequency changes, it is said to be the result of ultrasonic dispersion. This can occur when the medium of propagation is thin compared to the wavelength, or as a result of the material damping properties. In our work we deal with the latter which is called material dispersion. The scattering of an ultrasonic wave in contact with grains and interfaces of a polycrystalline material is the cause of attenuation and it creates dispersive velocities. Results of this analysis performed on the hot-rolled and laser-DED samples is shown in Fig. 3.4. It can be immediately observed that the hot-rolled sample exhibits a greater velocity value and lesser variation with frequency in contrast to the laser-DED samples. Furthermore, the build direction shows a lower value than the transverse directions.

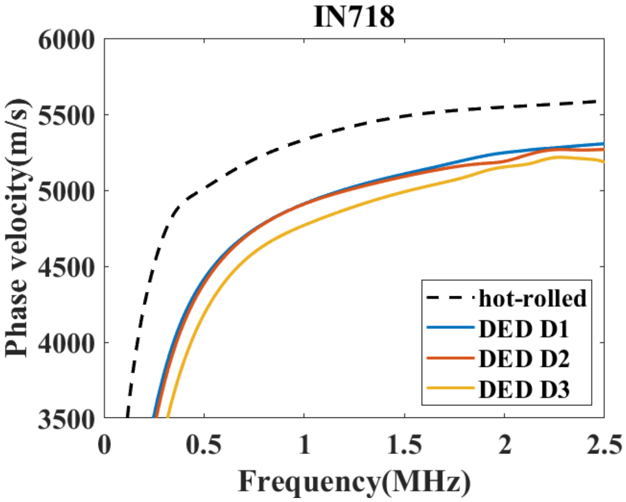

Figure 3.4. Phase velocity comparison between hot-rolled and laser-DED samples.

3.3. Ultrasonic attenuation coefficient

After observing the dispersive nature of the laser-DED, the attenuation coefficient was measured in order to quantify the wave energy losses in this medium, these results are compared to results from the hot-rolled sample.

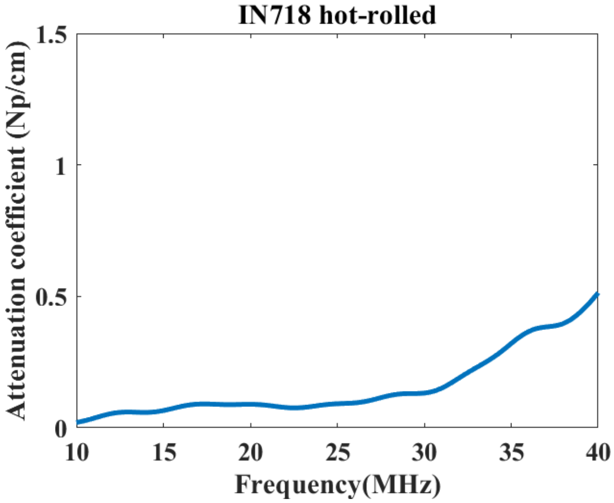

Figure 3.5. Ultrasonic attenuation coefficient of a hot-rolled IN718 sample.

The attenuation coefficient of the hot-rolled sample was measured with the immersion setup described in Ch. 2.2.2 this was measured with a 30 MHz immersion planar transducer. For a frequency range of 10 to 40 MHz, the attenuation values are low which agree with previous results for conventionally manufactured IN718 samples. The attenuation coefficient of the DED sample was measured using a 5 MHz planar immersion transducer. The magnitude of the values is much greater than those of the hot-rolled, for instance at 10 MHz the attenuation value of the laser-DED is 1.08 Nepers greater than for the hot-rolled. Furthermore, the attenuation curve exhibits peaks or humps which start at low frequencies.

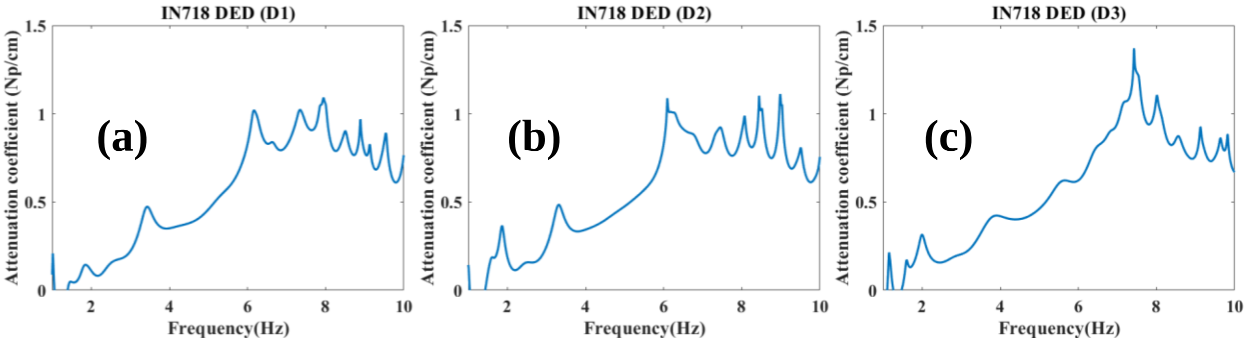

Figure 3.6. Attenuation coefficient (a, b, c) of IN718 DED sample in its three directions measured with a 5 MHz planar transducer.

3.4. Ultrasonic backscatter coefficient

The ultrasonic attenuation is attributed to several factors, among them, ultrasonic scattering is the most prominent. In order to quantify the losses of energy due to wave scattering, the backscatter coefficient was measured.

Similarly, as with the attenuation coefficient, the backscatter coefficient of the hot-rolled sample is low and again, this agrees to other reported results for conventional IN718 samples. The ultrasonic backscatter of the laser-DED samples is much larger than that of the hot-rolled sample. The 1-inch cube was measured with a 10 MHz focused transducer with focal distance equal to 4 inches. The three directions do not show a considerable difference in terms of magnitude, however, the presence of peaks at different frequencies can be observe. The backscatter noise in frequency domain also allows the comparison between the three directions, with the build direction having the greater magnitude of the peaks and happening around 5 MHz.

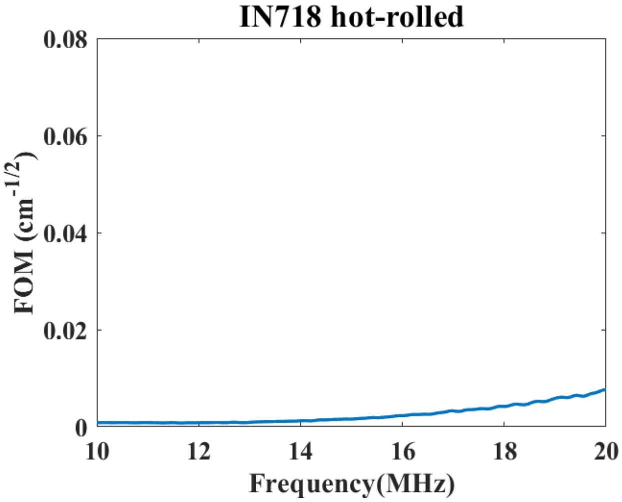

Figure 3.7. Backscatter coefficient of IN718 hot-rolled at 15 MHz.

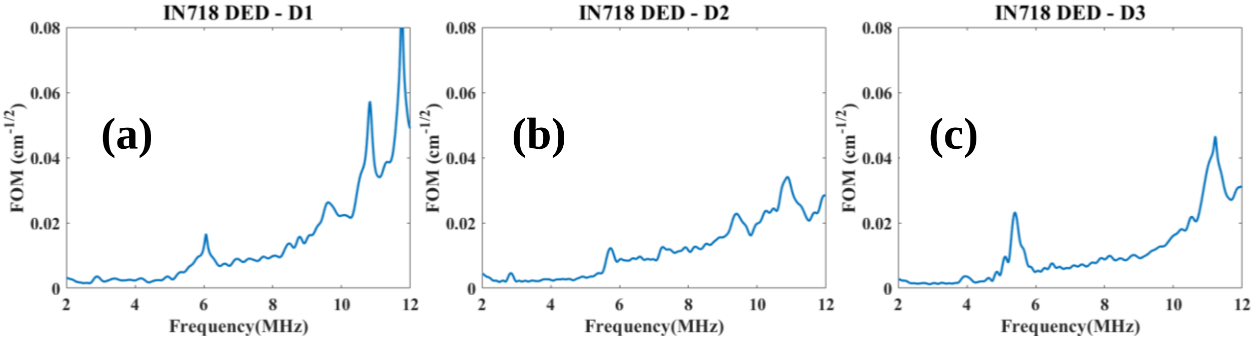

Figure 3.8. Backscatter coefficient (a, b, c) of IN718 DED sample in its three directions measured with a 10 MHz F=4in transducer focused at mid-plane.

3.5. Discussion

Micrographs from the hot-rolled and laser-DED samples were provided by our collaborators. For the former, the vertical direction (Z-direction) was analyzed as shown in Fig.

3.9. It was observed equiaxed grains with average size of approximately 15 microns. On the other hand, laser-DED micrographs show significant differences.

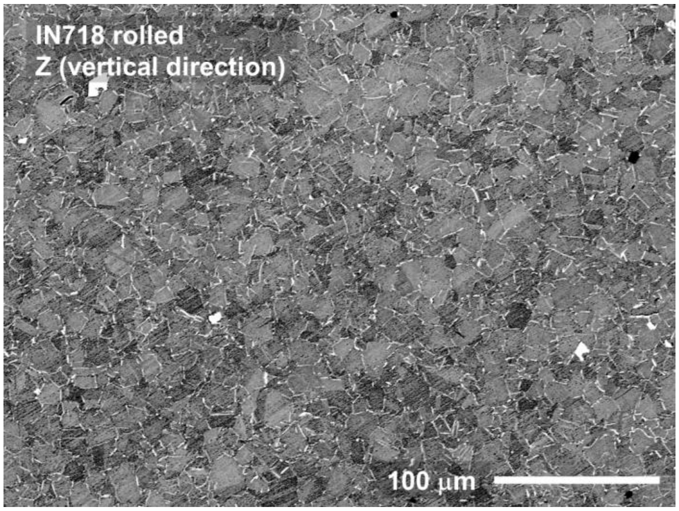

Figure 3.9. SEM image of IN718 hot-rolled sample along its rolling direction [12].

For the laser-DED sample, both the vertical or build direction (Z-direction) and the XY-plane were analyzed at different positions. Fig. 3.10 and Fig. 3.11 show these micrographs. As it can be observed, the micrographs show uniformity of the microstructure at different positions for a scale of 500 microns. Regarding the microstructure itself, the laser-DED sample present cellular and dendritic columnar grains (long slender grains) in all directions. They are a result of the temperature gradient and very high solidification rate of laser-DED process [13-16]. The melt-pool boundaries result in macro-grains of colonies of dendritic grains; in general, these micro-textured regions follow the build direction and would be of influence on the anisotropic properties of the laser-DED material. The size of these macro-grains range between 100 to 500 microns. Segregation of Mo and Nb, which are refractory elements, contribute to the major presence of Laves phase that surround the grains with a white outline as seen in Fig. 3.12. This figure shows the core of dendritic grains seen from the top of the sample perpendicular to the build direction. A relationship between the grain and macrograin sizes to the frequency where the scattering transitions from Rayleigh to stochastic can be made, this follows the fundamental Eq. 3.1.

$$\boldsymbol{\lambda} = \frac{\boldsymbol{v_{ij}}}{\boldsymbol{f}} \ldots \text{(Eq. 3.1)}$$

Where v_{ij} is the ultrasonic velocity and f is the frequency. The wave scattering mechanism depends on the interaction of the wave and the scatterer, being in our case the grains and macrograins. This interaction is dictated by the wavelength and average grain size difference. The average grain diameter is defined as $\overline{D} = 2\pi D$. When $\lambda \gg \overline{D}$, it is called Rayleigh scattering, this generally occurs at low frequencies. The next mechanism is stochastic scattering, and it is observed when the wavelength matches the average diameter, $\lambda \cong \overline{D}$. Finally, geometric scattering occurs when $\lambda \ll \overline{D}$.

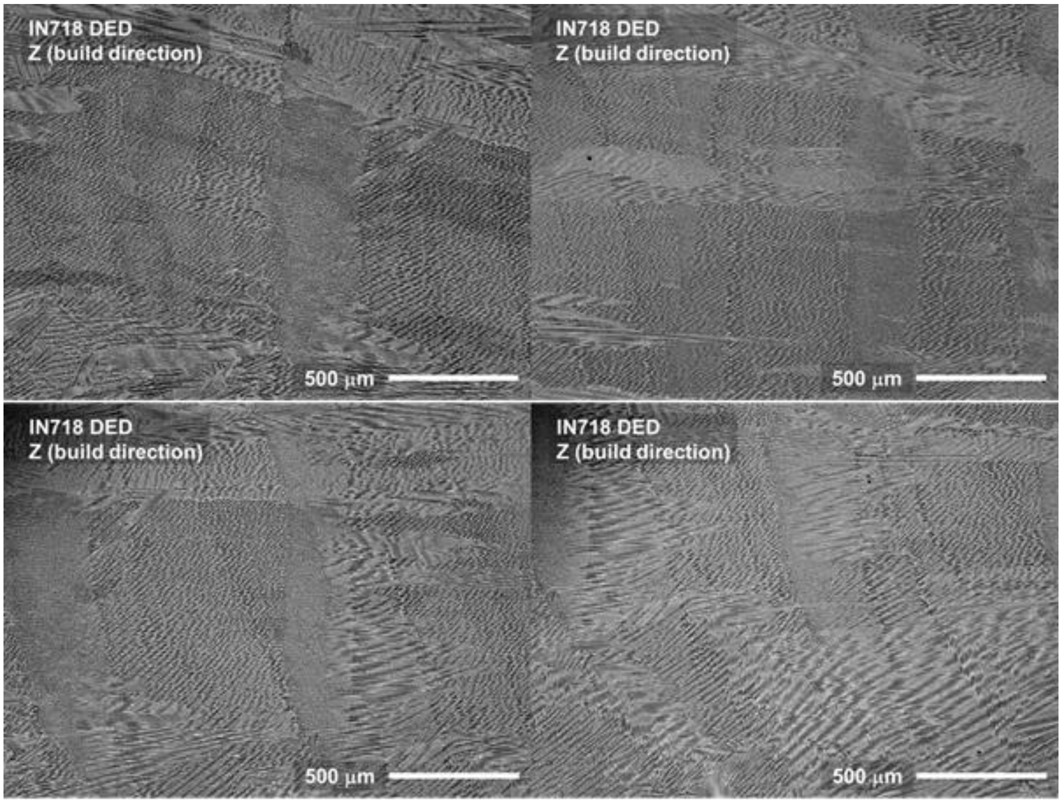

Figure 3.10. Micrographs of the IN718 laser-DED sample showing the build direction. Scale: 500 microns [12].

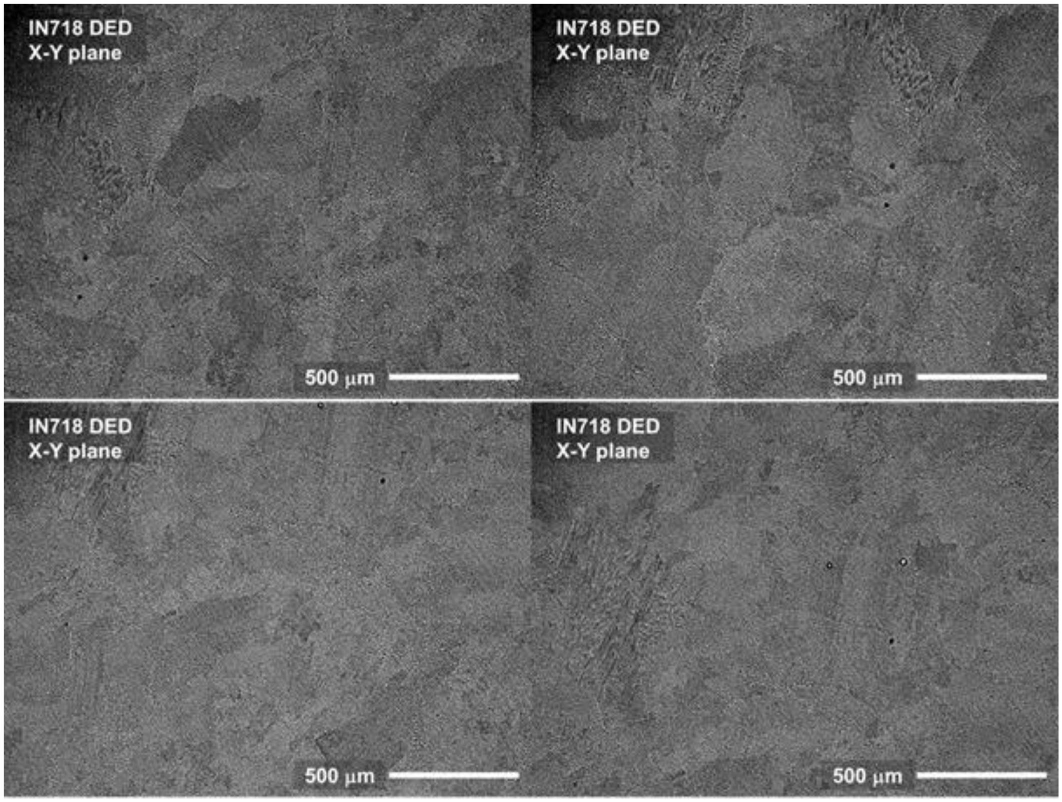

Figure 3.11. Micrographs of the IN718 laser-DED sample showing the XY plane. Scale: 500 microns [12].

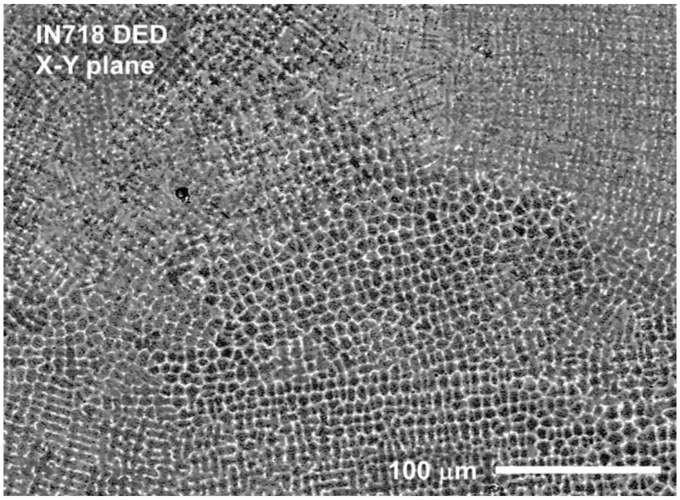

Figure 3.12. Micrographs of the IN718 laser-DED sample showing the XY plane. Scale: 100 microns [12].

Fig. 3.13 shows the (a) macrograin and (b) micrograin versus the frequency at which the scattering transition occurs, this helped us to understand the results from the frequency-dependent parameters.

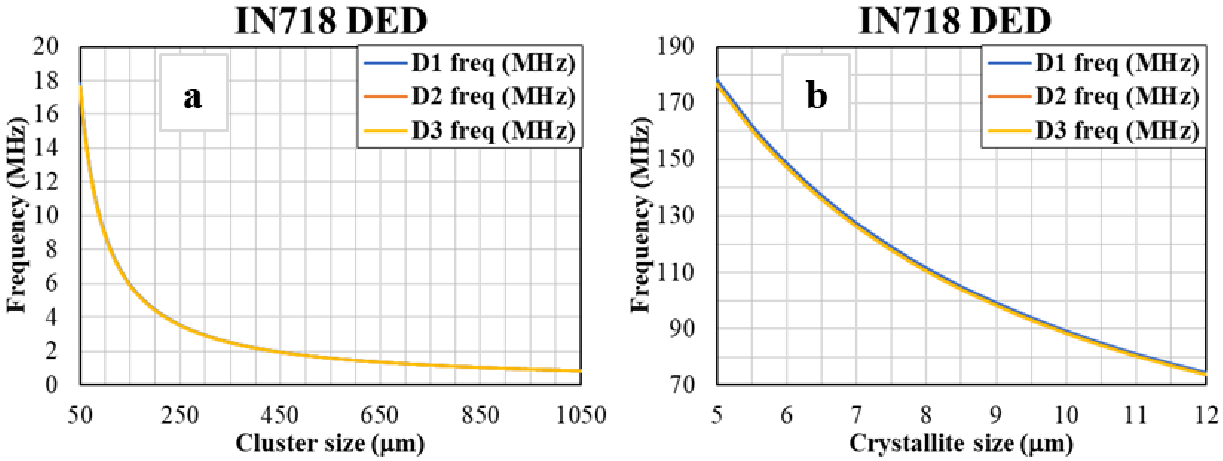

Figure 3.13. (a) macrograin and (b) micrograin relation to the Rayleigh-stochastic scattering transition frequency.

3.5.1. Elastic behavior

Laser-DED structures show epitaxial grow of dendritic columnar grains mainly parallel to the build direction. This crystallographic texture in the as-fabricated DED sample would affect the velocity since it is directly proportional to the Young's modulus along that direction making the velocity along the build direction the lowest, as the results showed. Furthermore, there can be observed in Fig. 3.12 a small black spot which is a carbide rich phase [12] that are known to have lower modulus, thus influencing the overall lower values for the laser-DED sample elastic constants. For a columnar grain, the fact that D2 is different than D1 shows that not all the grains follow the <001> direction (this can be observed in the micrographs), this is possibly a result of the solidification velocity in the 0° – 90° raster not being the same in the X and Y directions. Shear waves are more sensitive at the elastic anisotropy of the laser-DED sample. Fig. 3.14 shows B-scans of each direction for shear wave propagation at different angles of polarization, the shift in time of the greater amplitude as the polarization angle varies is due to a phenomenon called shear birefringence, this occurs when a polarized shear wave enters an anisotropic material, causing the split of the wave into two polarized waves. The transverse directions, D1 and D2, exhibit the greater birefringence, and peak amplitude in the build direction D3 remains almost constant in time. The fact that the build direction has different values from the other two directions reinforces the hypothesis of a strong crystallographic texture parallel to the build direction explained at the beginning of this Section.

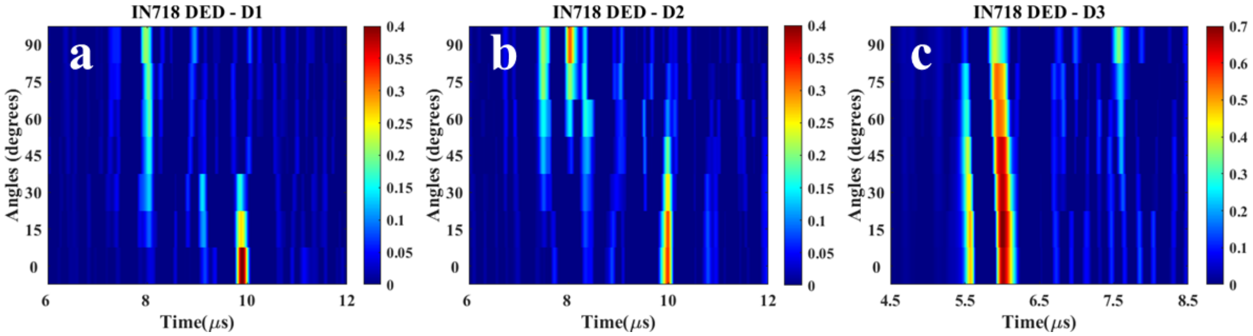

Figure 3.14. B-scan of shear wave birefringence (a, b, c) of the IN718 DED sample.

3.5.2. Ultrasonic attenuation coefficient

Perhaps the characteristic of the laser-DED microstructure that has a major influence on the frequency-dependent parameters is the presence of grain colonies. They can behave as a single grain when interacting with an ultrasonic wave and therefore, scattering at frequencies corresponding to those macrograin sizes. The attenuation coefficient results exposed the presence of “humps” which in essence are Rayleigh-stochastic scattering transition zones. The fact that they occur at low frequencies reinforces the hypothesis of the influence of the macrograins on the attenuation and also provides a greater picture of the macrograin size distribution not following a Gaussian distribution, given that there are humps at different frequencies, the lowest happening between 1.5 and 2 MHz which would correspond to macrograin sizes of 450 to 800 microns, according to the macrograin-frequency relation showed in Fig. 3.13. Another factor that would make the attenuation values of the laser-DED samples greater than the hot-rolled sample is the major presence of Laves phase in the former, since it has a large presence of the refractory elements Niobium and Molybdenum.

3.5.3. Ultrasonic backscatter coefficient

Scattering is the factor that has more influence on the attenuation. Similarly, as with the attenuation coefficient, the laser-DED sample showed greater values than the hot-rolled sample. Furthermore, the presence of steep backscattering peaks was also observed being the first time this behavior is experimentally reported. The frequencies where these peaks occur are fairly different than those of the attenuation coefficient, thus indicating a larger macrograin size distribution in the microstructure than what the attenuation coefficient can illustrate. Another important finding is that both the attenuation and backscatter coefficients in the build direction are greater than the transverse directions. Previous reports showed the anisotropy of these two parameters for columnar grains and macrograins [29-30]. In general, the attenuation coefficient values are greater when the wave propagates parallel to the columnar grain, this also occurs in our case. However, the backscatter coefficient is lower in the same direction since the interaction area perpendicular to the columnar grain is smaller than in the transverse directions, this does not agree with our findings where the three directions do not show a considerable difference in magnitude. The macrograins are microtextured regions that, in average, follow the build direction, our results would indicate that the macrograins are not exactly columnar grains; however, most of the dendritic and cellular grain colonies are textured along the build direction.

3.6. Conclusions

The work in this chapter shows the main differences in the ultrasonic response between AM (laser-DED) and conventional samples (hot-rolled). The hot-rolled sample does not show significant anisotropy; therefore, it can be simply considered as an isotropic sample. Its frequency dependent response shows low values in both the attenuation and backscatter coefficients. Moreover, the microstructure of this sample shows no variations in the microstructure and an average grain size of ~20 microns. This explains why the response of the frequency dependent parameters is small at the examined frequencies.

On the other hand, the laser-DED IN718 sample shows considerable anisotropy especially in both longitudinal and shear velocities. Also, the velocity value of the build direction is smaller in the case of longitudinal wave and greater in the case of shear wave, compared to the transverse directions. The frequency dependent parameters also show some variation along the three directions of propagation and are greater than the attenuation of the hot-rolled sample. However, the highlight of the results is the presence of humps in both the attenuation and backscatter coefficients, which are the result of the interaction of the ultrasonic wave with large clusters which in turn transform the scattering mechanism from Rayleigh to stochastic.

The progress of this work shows that ultrasonic parameters are sensitive to detect microstructural features found commonly in AM structures. Ultrasonic velocities illustrated the elastic anisotropy of the laser-DED sample which indicates microstructural texture mainly parallel to the build direction. Additionally, smaller elastic constant values in the laser-DED sample were a consequence of carbides having lower stiffness values. Attenuation coefficient quantifies energy losses and shows the presence of “humps” due to scattering transition zones (from Rayleigh to stochastic) at different frequencies which provides evidence of different average macrograin colony sizes in all the volume (not feasible with a single micrograph at the scales observed in this report). Backscatter coefficient shows peaks at different frequencies with a clear prominence when propagating parallel to the build direction. Furthermore, the fact that the attenuation coefficient is greater along the build direction and that the backscatter coefficients is does not show a difference in magnitude in the three directions would indicate that the microstructure is formed by macrograins of textured colonies of grains oriented parallel to the build direction. We can conclude that ultrasonic material characterization is an attractive contestant for nondestructive ex-situ qualification of laser-AM parts and would be ideal for setting a part qualification framework.

CHAPTER 4. ULTRASONIC NDE QUALIFICATION PARAMETERS FOR IN718 DED STRUCTURES

Qualification is defined as the evidence that a product design meets requirements in the presence of operational environments, and it can refer to a process, a machine, or a part [36]. A part can be qualified for a specific application by measuring physical properties with quantifiable parameters, for instance by measuring the modulus of metallic parts with destructive (tensile test) or non-destructive methods (ultrasonic characterization). These qualification procedures are compiled within standards and must comply with requirements specific to a certifying authority such as the American Society for Testing and Materials (ASTM), the International Organization for Standardization (ISO), the Federal Aviation Administration (FAA), the American Society of Mechanical Engineers (ASME) or the Aerospace Material Specifications (AMS). Among them, ASTM and ISO are leading the development of standards for the AM industry with the creation of the ASTM Committee F42 in 2009 and the ISO Technical Committee 261 in 2011 [45]. In order to avoid duplication of standards within the AM industry, these two institutions joined forces through a cooperative agreement. They continue working towards the development of standards related to terminology, design, materials and processes, and test methods of mechanical properties.

Regarding nickel-based superalloys, the standards F3055-14a and F3056-14a referring to Inconel 718 and Inconel 625 fabricated with powder bed fusion (PBF) technology, respectively, are intended for purchasers or producers and provide specifications for the acceptance of parts under the complying of minimum tensile properties, these standards do not mention specifications for non-destructive testing [40,41]. The standard F3187-16 is a guide for DED of metals that defines the requirements for this technology application such as space, set-up, process documentation or process monitoring technologies. In its section describing post processing it is mentioned that the ability to perform ultrasonic non-destructive testing can be affected by the unique microstructure of the part developed during deposition [39]. The standard F3122-14 specifies the evaluation of mechanical properties for AM metallic materials, it describes the destructive methods to quantify deformation (tensile test, uniaxial compression, bearing, bending, hardness, etc.) and fatigue (axial force fatigue test, fracture toughness, crack growth) properties, the standard does not mention non-destructive testing. The application of this standard can be affected by the AM material, anisotropy, porosity, testing environment, etc. [42]. More recently, and after years of preparation, the standard E3166-20 was published, this standard serves as a guide for NDE of after build AM metallic parts for aerospace applications. It discusses NDE methods applicable to aerospace parts fabricated via PBF and DED and includes nickel-based superalloys, among others. It also discusses the typical defects present in AM parts [43]. However, this standard does not provide a novel approach regarding ultrasonic testing, and it is limited to the methods described in the standards from the ASTM subcommittee E06.07 on ultrasonic methods. There is still a gap in the state-of-the-art of ultrasonic NDE qualification procedures for laser-processed nickel-based superalloys that can consider the challenges posed by the material microstructural features.

In this chapter, qualification parameters for laser-DED IN718 parts are proposed. These parameters quantify the anisotropy, microstructural heterogeneity, average cluster size and the grain or cluster size contribution to ultrasonic attenuation. The ultrasonic velocity, attenuation and C-scans of the samples are used as the basis for the derivation of the qualification parameters. Two laser-DED IN718 samples fabricated with different process parameters are evaluated to observe the influence of the laser power and scan speed have on the qualification parameters. The first sample fabricated at MSU is called PP1 and the sample fabricated at Optomec is called PP2, details regarding the fabrication of these samples is described in Ch. 2.1.1 and 2.1.2. These results are compared to those of a hot-rolled sample that can be considered as isotropic and homogeneous.

4.1. Proposed qualification parameters

4.1.1. Anisotropy index: A_{LS}

This proposed parameter quantifies the degree of elastic anisotropy in these IN718 samples, and its use can be further extended to characterize any metallic sample having any crystal symmetry where their ultrasonic velocities at their principal directions can be measured. This parameter has been based on the general elastic-anisotropy measure proposed by Ledbetter and Migliori [44], where their proposed anisotropy index is the squared ratio of the maximum and minimum shear velocities shown in Eq. 4.1. There, $v_{S_{ij}}$ represents the shear-wave velocity among all propagation and polarization directions.

$$A^* = \frac{\max\,({v_{S_{ij}}}^2)}{\min\,({v_{S_{ij}}}^2)} \dots \text{(Eq. 4.1)}$$

Since we observe changes in both longitudinal and shear velocities, we utilize the relationship between the maximum and minimum ultrasonic velocities as shown in Eq. 4.2. Compared to the anisotropy index defined earlier, we also notice that the variation between the longitudinal and shear velocities is not the same. Therefore, it becomes important to include both velocities to define a single parameter. Physically, this parameter will capture the maximum and minimum variation in the velocities induced by anisotropy. The advantage of our proposed parameter is that it is derived from the ultrasonic velocities propagating along the principal directions, thus, we get one parameter that simplifies the qualification process. This becomes particularly important in the case of as-fabricated laser-processed IN718 samples where the nature of the fabrication process is highly influenced by the processing parameters and the material, and results in samples with complex microstructures and different degrees of anisotropy [14].

$$A_{LS} = \frac{\max(v_{L_i})}{\min(v_{L_i})} \times \frac{\max(v_{S_{ij}})}{\min(v_{S_{ij}})} \dots \text{(Eq. 4.2)}$$

This anisotropy qualifying parameter can easily be tested where there is no anisotropy, i.e., $\max(v_{L_i}) = \min(v_{L_i})$ and $\max(v_{S_{ij}}) = \min(v_{S_{ij}})$. Therefore, in the absence of anisotropy, the ratio $A_{LS} \cong 1$. This will be evaluated for all the samples including a conventional hot-rolled IN718 sample.

4.1.2. Heterogeneity parameters: standard deviation (σ) and mean (μ)

The back-wall amplitude C-Scans will provide information that can be related to the microstructural heterogeneity of the as-fabricated laser-DED IN718 samples. Microstructural heterogeneity is defined as spatial variation of microstructural features such as grain morphology, i.e., shape and size, distribution of phases and other features. While this is expected to be small for conventional microstructures, we can observe a large spatial variation for the IN718 DED structures. The back-wall amplitude is affected by the ultrasonic attenuation of the wave energy as it travels through the sample. The major contribution to the ultrasonic attenuation is grain scattering; thus, if there is microstructural heterogeneity, then a spatial variation of the back-wall amplitude will be observed.

To extract parameters which are physically meaningful and represent the microstructures, it is important to utilize the heterogeneity of the ultrasonic response. Incidentally, heterogeneity is also the reason conventional NDE qualification methods fail for DED structures. In this work, we propose to utilize this heterogeneity to quantify the structure. To extract simple parameters from the data, we follow a simple image processing algorithm which involves extracting the histogram of the image, followed by determining the mean (μ) and standard deviation (σ) of the distribution which is expressed in Eq. 4.3.

$$G(dB) = Ae^{-\left(\frac{\mathrm{dB}-\mu}{\sigma}\right)^2} \ldots \text{(Eq. 4.3)}$$

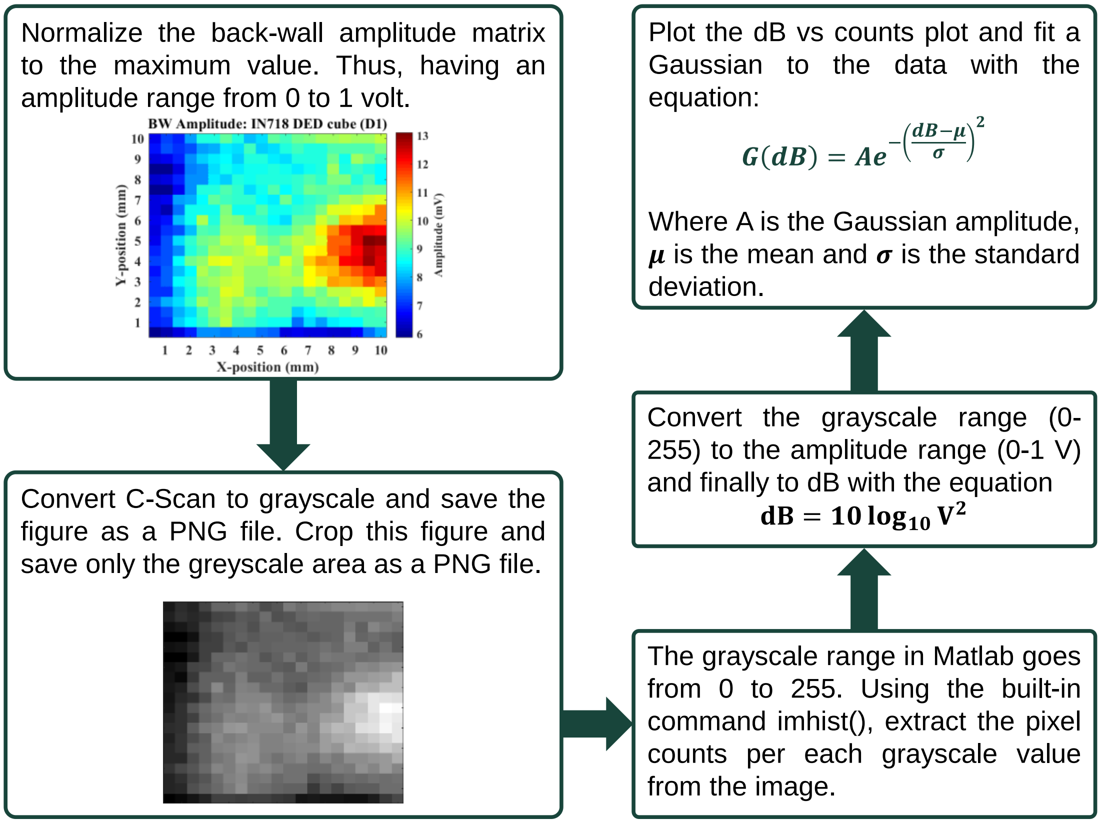

Normalize the back-wall amplitude matrix to the maximum value. Thus, having an amplitude range from 0 to 1 volt.

Convert C-Scan to grayscale and save the figure as a PNG file. Crop this figure and save only the greyscale area as a PNG file.

The grayscale range in Matlab goes from 0 to 255. Using the built-in command imhist(), extract the pixel counts per each grayscale value from the image.

Convert the grayscale range (0-255) to the amplitude range (0-1 V) and finally to dB with the equation

$$\mathbf{dB = 10\log_{10} V^2}$$

Plot the dB vs counts plot and fit a Gaussian to the data with the equation:

$$G(dB) = Ae^{-\left(\frac{dB-\mu}{\sigma}\right)^2}$$

Where A is the Gaussian amplitude, $\boldsymbol{\mu}$ is the mean and $\boldsymbol{\sigma}$ is the standard deviation.

Figure 4.1. Process to obtain the standard deviation (σ) and mean (μ) qualifying parameters from a back-wall amplitude C-Scan.

From a given amplitude C-Scan, and following the procedure described in the flowchart shown in Fig. 4.1, two parameters can be extracted that can be utilized to quantify the microstructural heterogeneity and the average wave energy loss: standard deviation (σ) and mean (μ). σ provides a metric to quantify the distribution of back-wall amplitudes and μ measures the average energy loss in the total area represented by the C-Scan.

4.1.3. Attenuation coefficient parameters: A and B

A general model to describe the ultrasonic attenuation coefficient is given by Eq. 4.4 [28-29,48].

$$\alpha_{model} = Af^4 + Bf^2 \ldots \text{ (Eq. 4.4)}$$

Where A and B are fitting coefficients to this model and serve to scale the contributions to the fourth and second power of the frequency. In general, and as it was mentioned in Ch. 4.1.2, the major contribution to the attenuation coefficient is grain scattering, and both parameters A and B quantify different grain scattering mechanisms, i.e., Rayleigh and stochastic scattering. Recalling the definition of these types of scattering mechanisms described in Ch. 3.5, the parameter A will contain contributions to grain scattering from small grains ($\lambda \gg \overline{D}$) and B will contain contributions to grain scattering from large cluster of grains ($\lambda \cong \overline{D}$).

As it was also discussed in Ch. 3.5, the as-fabricated IN718 laser-DED samples exhibited large cluster of small dendritic grains, ranging from 100 to 500 microns, making the two parameters A and B suitable to quantify their grain scattering contributions. Given that these microstructural features influence greatly the mechanical properties of the sample, we propose the use of the A and B attenuation fitting parameters as metrics to qualify laser-processed IN718 samples.

4.1.4. Ultrasonic scattering transition peaks: $P_{k\bar{d}=1}$

Without a doubt, the characteristic that make these laser-DED IN718 samples unique is the presence of large cluster of dendritic grains. When the ultrasonic wavelength matches the scatterer average size, which in this case occurs with the dendritic grain clusters at low frequencies from 2 to 10 MHz, a transition in the scattering mechanism from Rayleigh to stochastic occurs and it is exhibited in the form of peaks in the ultrasonic attenuation coefficient curve. The frequencies at which these transition peaks occur can be related to the average cluster size in the sample using the relationship $k\overline{d} = 1$, where the wavenumber is defined as $k = \omega/v_{ij} = 2\pi f/v_{ij} = 2\pi/\lambda$ and $\overline{d}$ is the average grain diameter; thus, this $k\overline{d} = 1$ relationship also takes the form $\lambda = \overline{D}$, where $\overline{D} = 2\pi\overline{d}$. Compared to optical microscopy where only a section of the surface can be sampled, ultrasonic imaging provides volumetric information. This allows the determination of the average cluster size of the entire volume of the sample by tracking the peak position. For example, processing parameters like laser power can result in changes to solidification rate, which will also change the average cluster size, which in turn will shift the transition peaks. Therefore, we choose the transition frequency as one of the parameters for qualification.

4.2. Results

4.2.1. Anisotropy index: A_{LS}

The degree of anisotropy was first characterized using the parameter A_{LS}. This was conducted for the two processing parameters PP1 and PP2. In addition, the conventional IN718 hot-rolled sample is also tested to demonstrate the isotropy of conventional samples compared to those fabricated with laser-DED AM. Fig. 4.2 shows the A_{LS} values of these samples of different fabrication.

The PP1 samples exhibit an A_{LS} value of 1.112 with a range from 1.098 to 1.131 whereas the PP2 sample A_{LS} is 1.298, i.e., 16.7% larger than PP1. The hot-rolled sample A_{LS} is 1.006 which is closer to the theoretical isotropic value $A_{LS} = 1$. Table 4.1 summarizes the percentage difference between the theoretical and the tested A_{LS} and it clearly shows the significant anisotropy of the laser-DED samples and the importance of the A_{LS} parameter as a qualifying tool to differentiate between two processing parameters.

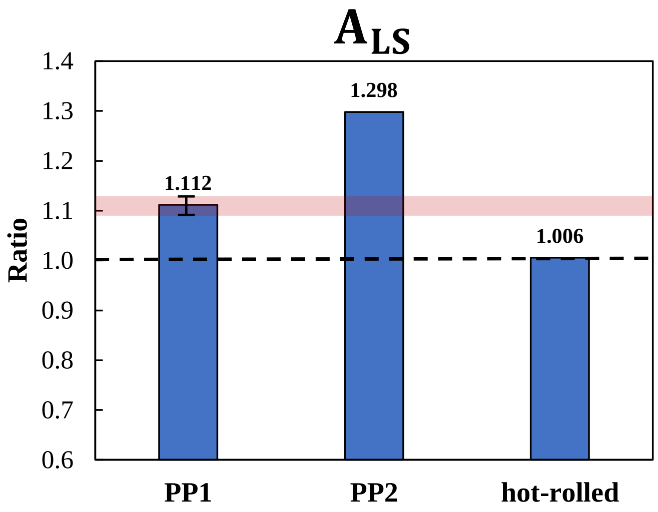

Figure 4.2. Anisotropy index of the laser-DED samples PP1 and PP2 compared to a hot-rolled sample.

IN718	A_{LS}
PP1	11.199
PP2	29.780
hot-rolled	0.560

Table 4.1. Percentage difference between A_{LS} of samples and $A_{LS} = 1$.

4.2.2. Heterogeneity parameters: standard deviation (σ) and mean (μ)

The standard deviation (σ) and mean (μ) heterogeneity parameters were extracted from C-Scans of the different samples using the procedure described in Fig. 4.1. In the case of the PP1 sample, amplitude C-Scans for the three principal directions of propagation were analyzed. This produces a range of values for both σ and μ heterogeneity parameters for the PP1 sample. The C-Scan of the build direction of the PP2 sample exhibited more variation, having an area with significantly lower back-wall amplitudes. The waveforms from this area presented a large-amplitude echo between the front-wall and back-wall echoes which affected the amplitude of the back-wall echo, given that a large percentage of energy was being reflected to the immersion transducer before the wave reached the back-wall of the sample. This motivated the decision to analyze two separate amplitude C-Scans of the PP2 sample: a “good area” where the middle echo was not present, and the “full area” which is the complete amplitude C-Scan. Lastly, the C-Scan of the hot-rolled was analyzed. We can observe that it shows considerably lower heterogeneity compared to the DED samples. Fig. 4.3 shows the six back-wall amplitude C-Scans that were analyzed.

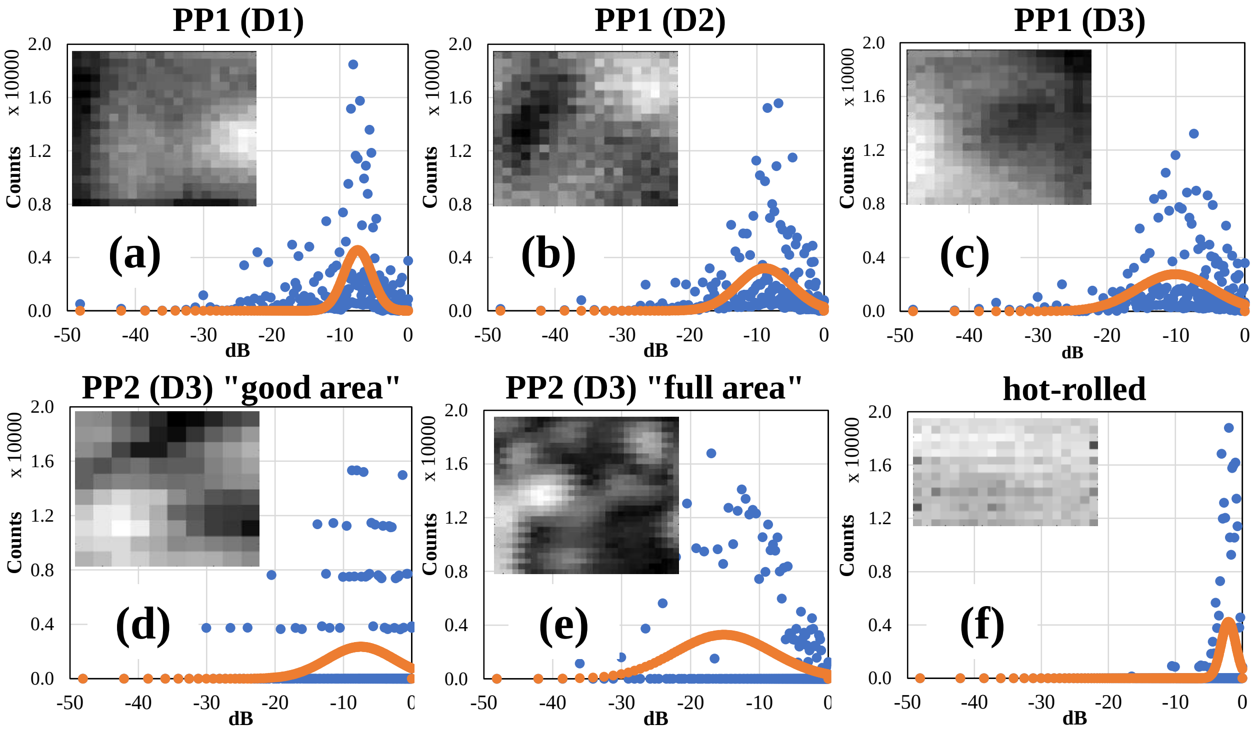

Figure 4.3. Grayscale backwall amplitude C-Scans and their corresponding pixel counts and Gaussian distribution plotted against energy loss represented in decibels.

The σ and μ parameters shown in Fig. 4.4 were extracted using Eq. 4.3. Describing first the standard deviation σ, the PP1 sample has a σ of 5.54 dB ranging from 2.89 dB to 7.72 dB, with the highest value corresponding to its build direction. The PP2 “good area” σ equal to 7.03 dB falls within this range and it is close to the PP1 build direction σ, only differing by 9.84%. The

PP2 “full area” σ value of 9.97 dB falls outside of the range with a difference of 41.76% in relation to the “good area” σ. This is evidence of the influence that different processing parameters have on the microstructural heterogeneity of IN718 laser-DED samples, in this case by presenting an area with large amplitude middle-echoes that are detrimental to the back-wall echo amplitude. The hot-rolled σ is small even compared to the lower limit of the PP1 σ values with a difference of 87.05%, this small σ is expected from a conventional sample where microstructural heterogeneity is insignificant.

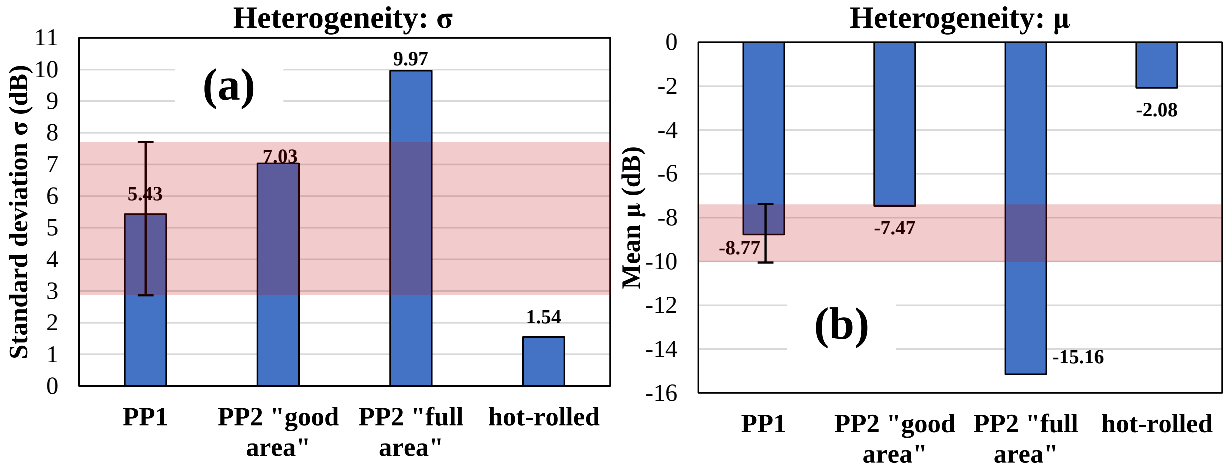

Figure 4.4. Heterogeneity parameters σ (a) and μ (b) of the PP1, PP2 and hot-rolled samples.

The PP2 “good area” μ parameter equal to -7.47 dB falls within the PP1 μ window that ranges from -7.38 dB to -10.13 dB. In this case, and opposite to what occurred with the σ parameter, the PP2 “good area” μ value is closer to the lower limit of the PP1 range with a difference of 1.15%; however, it differs by 35.63% from the upper limit of PP1 range that corresponds to the build direction. Thus, the PP2 build direction “good area” exhibits a lower average energy loss than the PP1 build direction. The PP2 “full area” μ value of -15.16 dB is also outside of the PP1 μ range and its energy loss is 102.97% times greater than that of the “good area”. The hot-rolled μ value of -2.08 dB is the lowest of the group with an enormous difference of 255.34% compared to the lower limit of PP1.

4.2.3. Attenuation coefficient parameters: A and B

Polynomial curves of the model expressed in Eq. 4.4 were used to fit the experimental attenuation coefficient data of the DED samples in the frequency range from 2 to 7 MHz, given that a 5 MHz transducer was used to conduct the experiments. The hot-rolled sample attenuation coefficient was measured with a 30 MHz transducer; therefore, the frequency range from 10 to 40 MHz was used to fit the attenuation model. Fig. 4.5 shows the attenuation coefficient curves and their corresponding fitted attenuation models for PP1, PP2 and hot-rolled samples. The figure also shows scattering transition peaks in the attenuation coefficient of the DED samples, this will be later used to calculate another qualification parameter.

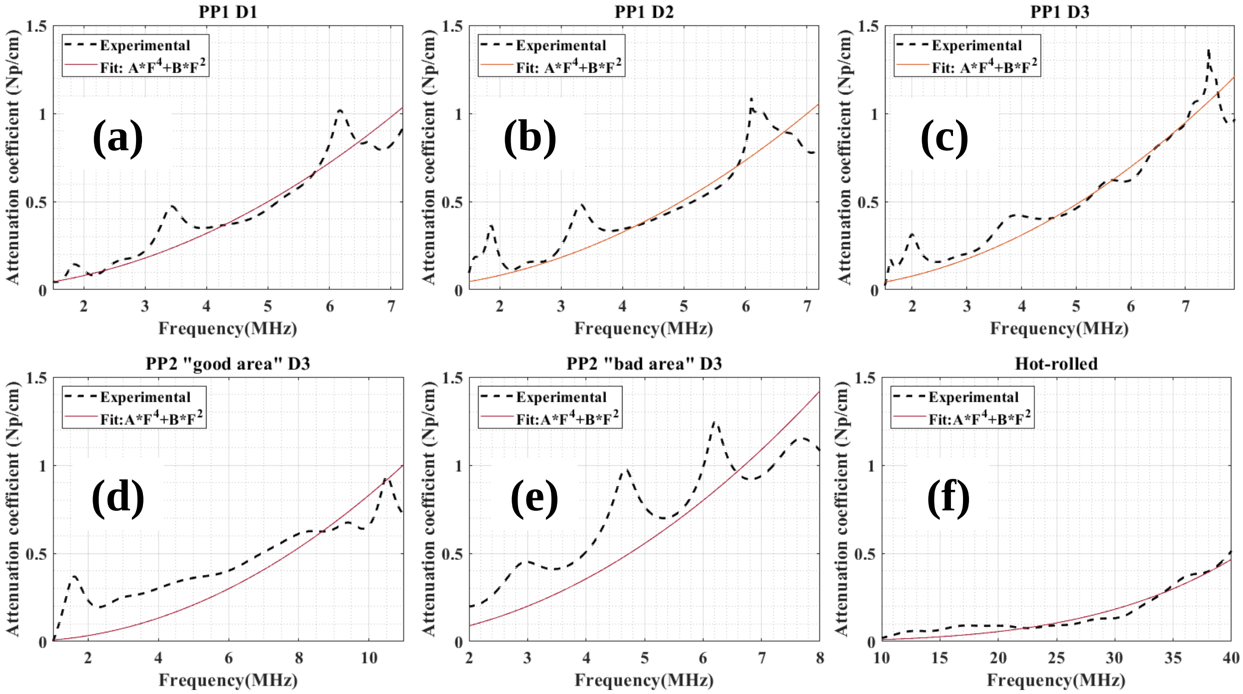

Figure 4.5. Ultrasonic attenuation coefficient and the corresponding attenuation model fitted for the samples PP1, PP2 and hot-rolled.

The PP2 “good area” follows the same definition as for the heterogeneity parameters, where the attenuation coefficient was calculated for one of the locations where the large amplitude middle-echo does not appear. In a similar fashion, the “bad area” attenuation coefficient was calculated from one waveform of the region where this middle-echo appears. Fig. 4.6 shows the comparison between PP1, PP2 “good area” and PP2 “bad area”. The quartic term A of the PP2 “good area” equal to 3.74×10^{-12} falls within the range of values of the PP1 sample that goes from 3.16×10^{-12} to 7.29×10^{-12}. Conversely, the PP2 “bad area” A parameter value of 2.62×10^{-12} is below than the lower limit of the PP1 range. The case of the quadratic parameter B is different where both PP2 areas fall outside the PP1 window ranging from 1.94×10^{-2} to 2.04×10^{-12}. The DED sample parameters are in a completely different scale than the hot-rolled sample A and B parameters equal to 1.26×10^{-7} and 8.95×10^{-5}, respectively.

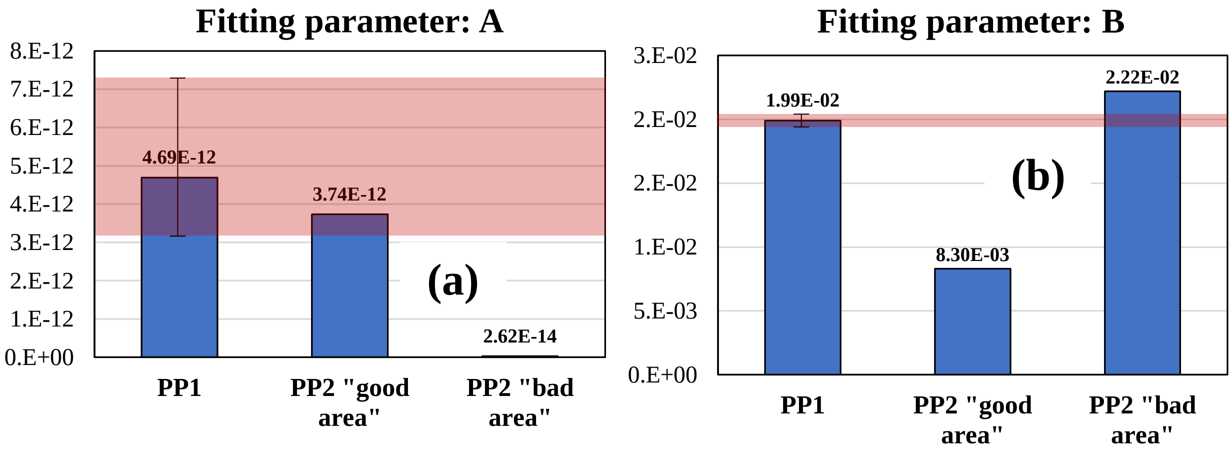

Figure 4.6. Attenuation model $\alpha(f_{MHz}) = Af^4 + Bf^2$ fitting parameters A (a) and B (b).

4.2.4. Ultrasonic scattering transition peaks: $P_{k\bar{d}=1}$

Using the transition peak locations of the three directions of the PP1 sample and of the PP2 sample from the attenuation coefficient curves shown in Fig. 4.5, and the expression $k\bar{d} = 1$ that complies with the Rayleigh to stochastic scattering mechanism, the average cluster sizes of each transition peak can be determined.

In this case, only the prominent peaks were considered, and the results were combined for each sample, i.e., the three directions of PP1 and both cases of the PP2 build direction. Table 4.2 shows the relation between frequency and cluster size for both samples.

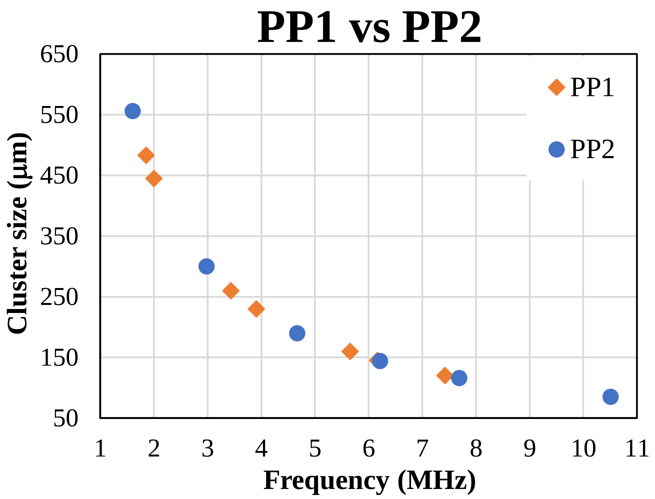

Figure 4.7. Average cluster size of the PP1 and PP2 samples as a function of the frequencies where the peaks appeared.

PP1		**PP2**	
Freq (MHz)	**Avg cluster size (µm)**	**Freq (MHz)**	**Avg cluster size (µm)**
1.854	483	1.602	556
1.999	445	2.98	300
3.433	260	4.671	190
3.906	230	6.213	144
5.653	160	7.69	116
6.165	145	10.51	85
7.423	120		

Table 4.2. Scattering transition frequencies and corresponding average cluster size.

It is worth noting that the selected transition peaks are not the only ones present in the attenuation curve; however, their prominence occurs due to a greater number of clusters having similar sizes. Numerical studies have shown that the width of the peak is related to the distribution of grains of a particular size range; thus, what differentiates a prominent transition peak from a smooth transition peak is the larger or fewer concentration of grains [47].

4.3. Discussions

The reviewed proposed qualification parameters serve to quantify different aspects of laser-processed IN718 that most of the standard qualification procedures fail to accomplish for such complex materials. The A_{LS} parameter is very similar to the anisotropic index, which has been used with a great deal of success to quantify the anisotropy. The A_{LS} results suggest that hot-rolled sample agrees well with the isotropic value of ~1, and the PP1 sample has a small overall variation of 3.00% (1.112 ± 0.014). The fact that this average lies away from 1 signifies the anisotropy of the PP1 structure. More importantly, PP2 seems to have a higher anisotropy factor, which is farther away from 1. This suggests that the A_{LS} parameter that we defined is sensitive to changes in the microstructure resulting from different processing parameters.

It can be argued that the microstructural heterogeneity of this complex IN718 DED material is the main reason characterization with most qualification standards becomes impossible. By extracting two parameters, σ and μ, from the ultrasonic C-Scans which contain volumetric information of the sample, the heterogeneity can be quantified. Furthermore, this is the first heterogeneity parameter ever quantified and it is our belief that its adoption as a qualifying parameter for complex materials such as laser-processed nickel-based superalloys will be of significant importance in order to understand how different fabrication processing parameters influence microstructural heterogeneity. Its disadvantage is that since its calculation is only based on amplitude C-Scans, it does not provide information regarding the physical and chemical nature of the heterogeneity. For instance, it is important to note that in the so-called "bad region" in the PP2 sample, a strong reflection was observed at half-thickness. This suggests that there might be a large defect at the center of the sample. However, in a previous example, we had machined and cut the sample at a similar "defective spot" and did not notice any defect even under microscopy. Therefore, the origin and nature of the bad region is debatable, and we assume that the general area has a different set of properties, which is reasonable.

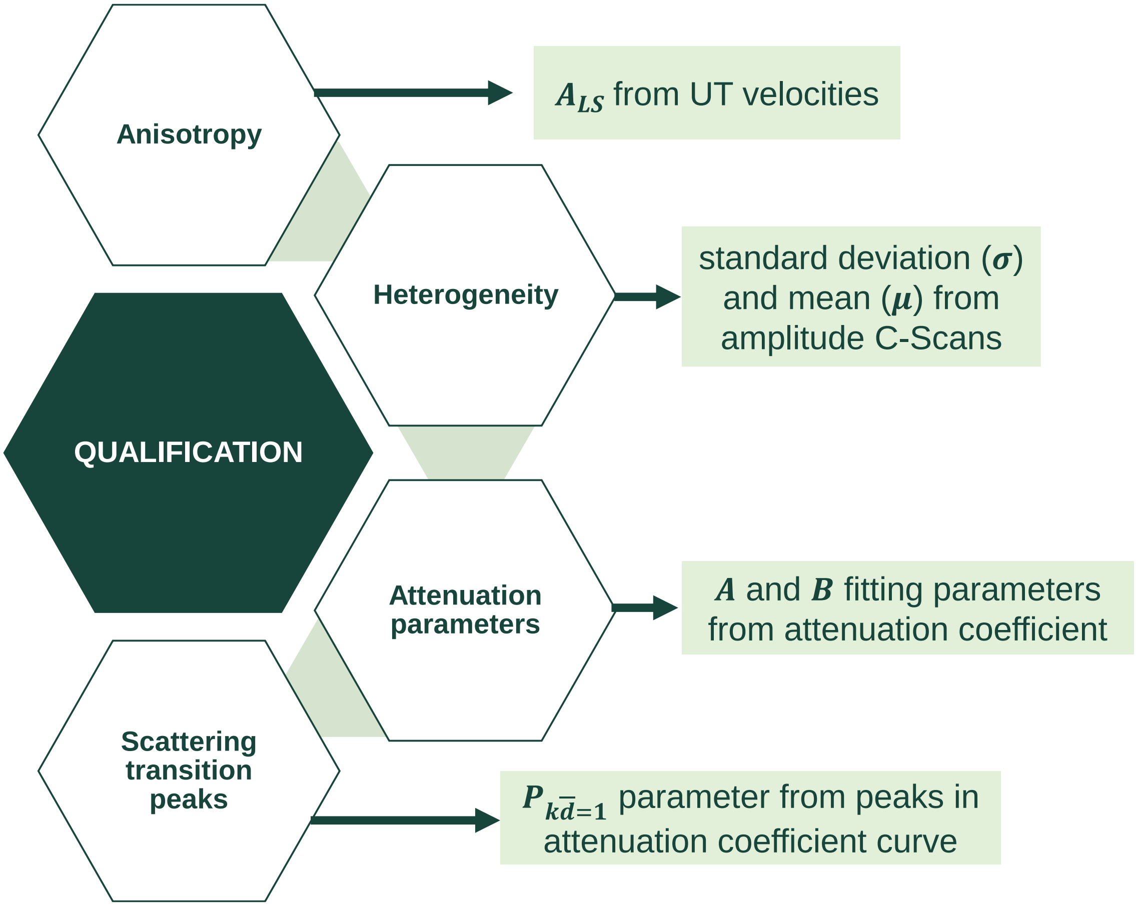

Figure 4.8. Identified qualification parameters and their metrics obtained from ultrasonic NDE characterization.

The A and B parameter from the attenuation coefficient model $\alpha_{model} = Af^4 + Bf^2$ quantify the different grain scattering mechanism contributions from the grains and its application for the DED IN718 samples showed interesting results. The A (quartic) parameter quantifies grain scattering in the Rayleigh regime, which in the case of the tested DED samples occurs from the cellular and dendritic columnar grains of average grain diameter of approximately 10 microns, complying with the condition $\lambda \gg \overline{D}$. Both the PP1 and PP2 "good area" have similar values, however the PP2 "bad area" has a lower value due to the fact that its major contribution to scattering occurs in the stochastic regime. The B parameter quantifies the stochastic scattering contribution to ultrasonic attenuation with the condition that $\lambda > \overline{D}$. PP1 value is closer to PP2 "bad area" value than to the PP2 "good area"; however, the PP2 "bad area" waveform presents a strong reflection at half-thickness which will also contribute to this B parameter. The B parameter of the PP1 sample is one order of magnitude greater than the PP2 "good area" (139.75% times greater) which would indicate that the PP1 sample has a greater number of clusters that comply with $\lambda > \overline{D}$. The challenge with consistently using this parameter is inability to fit the model equation with a good R^2 value. As the peaks become sharper and larger, the goodness of fit will decrease, which will make it challenging to get consistent fit parameters for comparison.

The scattering transition peaks $P_{k\overline{d}=1}$ contain volumetric microstructural information about the sample. Since the peaks occur at frequencies when the wavelength matches the average cluster diameter, $\lambda = \overline{D}$, it becomes easy to identify the average cluster sizes that are present in the structure. We believe this can become a critical tool in evaluating the grain structure using NDE. However, the transition peaks cannot be observed in the 1 – 20 MHz frequency range for most conventional measurement method since the grain size is small and does not satisfy the $\lambda = \overline{D}$ condition. However, this will be valid for IN718 samples, which have large grain clusters. Therefore, the transition peaks can play a significant role in qualification of as-fabricated IN718 DED structures.

4.4. Conclusions

It has been shown that the ultrasonic response from a laser-processed nickel-based superalloy can be utilized to derive parameters to quantify anisotropy, microstructural heterogeneity and size of cluster of grains. Also, these parameters are sensitive to microstructural variations that result from different processing parameters (laser-power and scan speed). Furthermore, these proposed parameters can be applied to qualify complex materials such as those used in the aerospace industry. We believe that these qualification parameters will contribute to the efforts of understanding the relationship between processing parameters and structural integrity.

CHAPTER 5. ULTRASONIC CHARACTERIZATION OF SS420-IN718 MULTI-MATERIAL STRUCTURES FABRICATED USING LASER DIRECTED ENERGY DEPOSITION

Recent progress in manufacturing has made it easier to fabricate near net complex shapes and geometries with minimal need for subtractive methods like machining. Specifically advanced manufacturing methods such as in-situ, laser processed methods including Powder Bed Fusion (PBF) and Laser Directed Energy Deposition (DED) have been utilized to build structures in a layer-by-layer fashion. Unlike traditional manufacturing process, in-situ 3D printing methodologies can give rise to complicated microstructures which are dependent on the processing parameters and geometry. There is large body of work that is being developed in the area of material characterization of additive structures [22,50-56]. Within this, one specific area that has received less attention is the use of the Laser DED technique for in-situ multi-material fabrication [57-61]. Laser DED has the ability to mix and combine different metallic powders, and deposit on a substrate. This allows us to fabricate a multi-material structure which can transition between two dissimilar materials using a transitional zone (composite mixture) of these two materials. In theory, a mixture of two dissimilar metals should have a gradual change in material properties. However, in most cases, the transition zone is the weakest point. A complete understanding of transition zone is required since many engineering components can be simplified via multi material structures, leading to minimum material usage, reduce manufacturing time and steps as well as provide multi-functionality. Also, the mixture of the two dissimilar metals may lead us to construct composite structures with balanced properties such as corrosion and wear resistance. Furthermore, the composite nature of these structures will also be useful for several applications including structures with localized properties, and compositionally and functionally gradient structures which are very relevant to acoustic metamaterials.

Compared to pure DED structures, multi-material DED structures can have very complex microstructures including segregation of different metastable phases [58-59,61], dendrite grains [12,58], etc. Traditionally, these structures have been characterized using destructive methods, which provide very local properties. There is a strong need to characterize these materials using volumetric methods to get average bulk response. Additionally, there is strong interest in just the nondestructive evaluation of these structures.

There is a large body of work starting from 1960s which has utilized ultrasonics waves to characterize the microstructure of polycrystalline materials. As the ultrasonic wave propagates through the material, the ultrasonic characteristics, i.e., speed and attenuation can be directly correlated to the microstructure. The velocity is a function of the elastic properties of each grain, and the orientation of the grains [62]. This allows us to characterize the anisotropy of the structure in a nondestructive manner. The ultrasonic attenuation coefficient has been used to characterize lattice defects across multiple length scales ranging from point defects and dislocations to average grain size [63,64].

In general, the attenuation is a result of absorption and scattering of ultrasonic waves as it propagates through a structure. In addition to the attenuation coefficient, we can also use backscatter coefficient, which characterize the grain noise, or backscatter from the grains [64]. These classical parameters have been traditionally used to characterize the microstructural features of metallic structures [65-67]. Recently, they have also been used to characterize additively fabricated structures [22,68-70]. The objective of this work is to characterize multi-material metallic composite structures fabricated in-situ using Laser DED technique. While researchers have demonstrated the ability to fabricate multi-material structures, there is very limited work on the nondestructive characterization of these materials. There are very few articles which have explored ultrasonic wave propagation in complex microstructures with meta-stable phases with multiple phases. In our humble opinion, this article is the first to measure and report the ultrasonic properties of such complex laser processed microstructures. Our focus is to utilize the ultrasonic properties to further understand the microstructural characteristics of the multi-material structures. We believe this will lead us to understand the bulk solidification dynamics of the structures in a nondestructive manner. Specifically, this article utilizes velocity, attenuation, and backscatter coefficients to characterize the additively fabricated structures. Additionally, the elastic anisotropy was characterized using the elastic constants measured from velocities. Finally, destructive analysis including hardness measurements, X-Ray diffraction and Scanning Electron Microscopy (SEM) images collected by our collaborators were used to interpret the ultrasonic results.

5.1. SS420-IN718 multi-material structures

Recalling the description of the fabrication of the multi-materials in Ch. 2.1.2, five SS420-IN718 laser-DED samples with mass percentage variation were used. These samples were fabricated at Optomec. The final dimensions of the samples were 25 mm (L) X 25 mm (W) X 19 mm (H), being the latter the build direction. The density was measured with the Archimedes method consisting of weighing the sample in air, followed by weighing it in fluid. The measured densities of the samples are given in Table 5.1.

Samples	**100% SS420**	**25% IN718**	**50% IN718**	**75% IN718**	**100% IN718**
Density (kg/m^3)	7879 ± 1	7949 ± 3	7989 ± 2	8038 ± 1	8248 ± 4

Table 5.1. Mixed samples densities measured with the Archimedes method.

5.2. Experimental details of ultrasonic testing

Ultrasonic characterization was conducted using two setups: contact-based setup for measuring velocities and immersion-based setup for attenuation and backscatter measurements. Details of each method and the measurement protocols are given below:

5.2.1. Ultrasonic velocities

The contact-based setup consists of a pulser/receiver which sends a broadband spike input to a narrow band contact transducer with acrylic delay. The longitudinal wave measurements were conducted at 5 MHz and shear wave measurements were carried out at 2.25 MHz. All the contact measurements were carried out in pulse-echo mode. The first and second backwall, i.e., reflections from the back of the sample were digitized at a minimum of 1 GHz using an 8-bit oscilloscope and post-processed in MATLAB to determine time of flight. To measure the group velocity of the samples, the analytic or envelop of the waveforms were calculated using Hilbert transform, and the time difference between the peaks of the envelopes were measured. Knowing the propagation path, the velocity can be measured directly. Shear wave transducers have a fixed polarization direction. To measure the anisotropy, the shear transducer polarization direction was rotated by $\pi/2$ and the velocity was measured.

5.2.2. Ultrasonic attenuation coefficient

The ultrasonic attenuation coefficient was determined using a broadband immersion setup [71]. Typically, this type of measurement is conducted in the far-field to get consistent amplitudes and using focused transducers. However, in this work we chose to use planar transducers. The main reason was to work around the large spatial inhomogeneity that we observe in the DED samples.

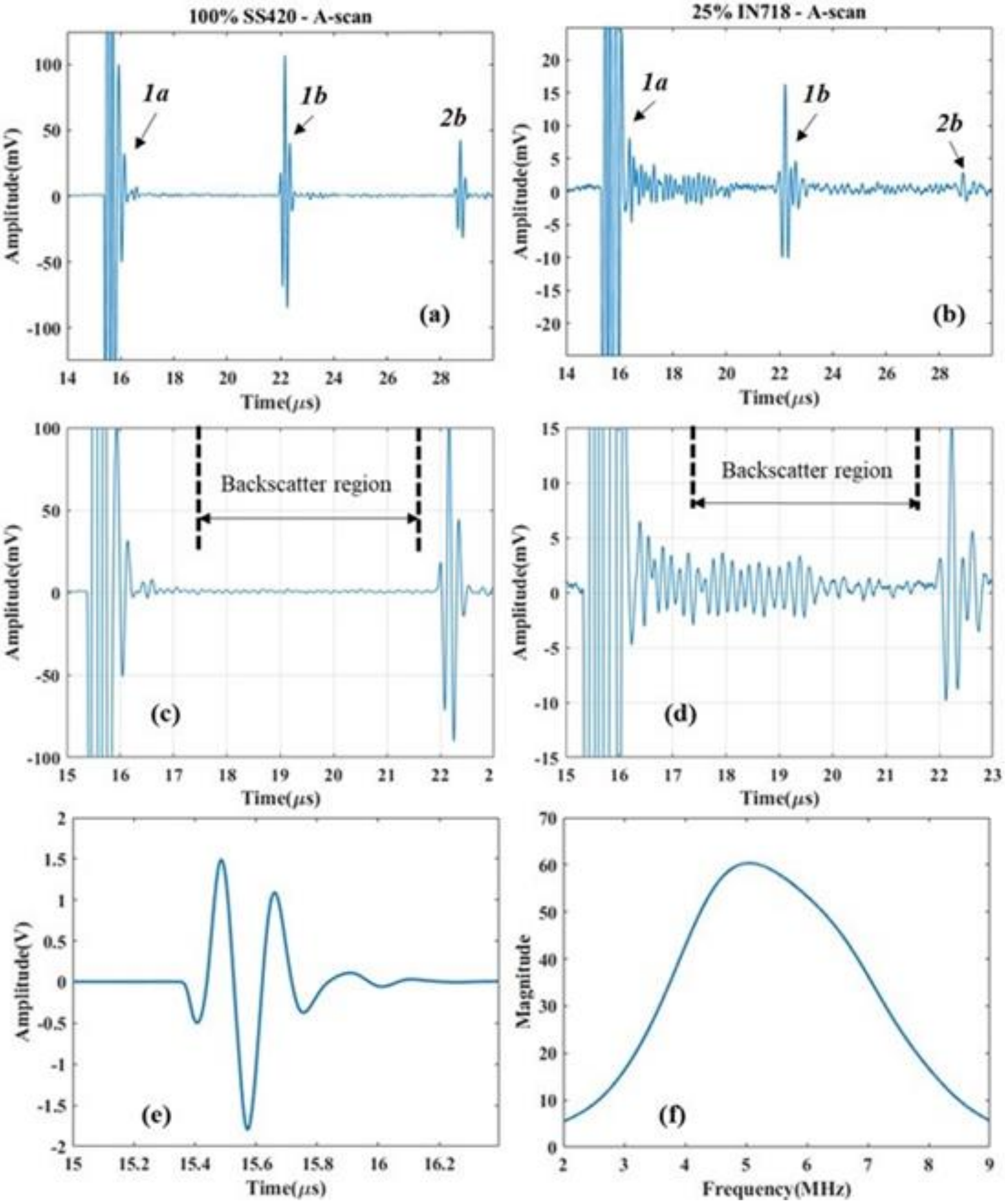

Figure 5.1. A-Scan showing the multiple echoes from the samples after immersed in water; (a) 100% SS420, and (b) 25% IN718. The backscattered amplitudes and the region chosen for processing the backscatter coefficient for (c) 100% SS420, and (d) 25% IN718. To show the relative backscattered amplitudes, the backwall is also shown. (e) A-Scan showing the reference echo to capture the transducer response, and (f) spectral response of the reference echo which was used for the backscatter coefficient determination.

Preliminary planar probe C-Scans suggested that the microstructure is highly inhomogeneous (in all directions) compared to conventionally fabricated structures. When using a focused transducer, we get a spatially dependent focusing gain between the starting and end point of the processing window. While this works well for conventional samples where the spatial inhomogeneity is small, if we have large variability in the microstructure as shown in Fig. 3.10, Fig. 3.11, and Fig. 3.12, the focusing gain can further complicate the results. Our objective was to highlight only the spatial variability of the sample. Therefore, we chose the planar transducer whose spatial/diffraction characteristics decay with propagation distance.

The immersion experiment is described in Ch. 2.2.2. The first and second reflections were used to calculate the attenuation coefficient as shown in Eq. 2.7. The attenuation measurements were carried out using a 5 MHz, 0.5 inch diameter immersion transducer. The received signal was digitized using a 12-bit digitizer at a sampling rate of 250 MHz. We chose a time window for the backwall such that the signal was positioned at the center of the window and any DC offset was minimized by using cosine windows.

5.2.3. Ultrasonic backscatter coefficient

The ultrasonic backscatter measurements were conducted using a 5 MHz planar transducer. Once again, these experiments are usually conducted using a focused transducer, with the focal spot positioned at half-plane of the sample. For the reasons described at Ch. 5.2.2, we chose to use the planar transducer. However, we made sure that the position of the processing window was in the far-field.

The forward propagation in water path was 11 mm, and the near-far field transition occurs at 17 mm of combined propagation (fluid + solid), i.e., 8.73 μs. For the pulse echo mode, this is equivalent to ≈ 17.5 μs. Therefore, the processing window started at 17.5 μs and ends just before the backwall, as shown in Fig. 5.1 (c) and d. A 10 mm X 10 mm scan was conducted at the center of the sample, with 0.5 mm scan resolution. To ensure we do not get any edge effects, the beam diameter at the end of the forward propagation should be within the sample. If the forward beam folds onto itself, it can cause additional phase aberrations. The beam width at the end of the forward propagation was calculated as 14 mm using Gaussian beam model. The backscatter scans were carried out at the center of the sample.

5.3. Rule of mixtures (RoM)

Since the mixture samples are a composite of two different materials, we will use a simple rule of mixtures formulation to determine the change in elastic properties, as well as ultrasonic velocities. We assume the structures are linear isotropic and use the theoretical weight fractions for all the analysis. The weight fractions can be written in terms of volume fraction and the densities as:

$$w_i = v_i \frac{\rho_i}{\rho_c} \ldots \text{(Eq. 5.1)}$$

where, $w_i = W_i/W_c$, is the weight fraction of each component, ρi is the density of each component, and $v_i = V_i/V_c$ is the volume fraction of each component.

Each component is represented by subscript "i", and the composite by subscript "c". Knowing the individual and composite densities, we can use Eq. 5.1 to get the volume fractions of IN718 and SS420. The total volume fraction is given by: $v_{ss} + v_{in} = 1$. We do not consider voids in this equation and will explore it in a different analysis. We can now use the well-known Voigt-Reuss-Hill estimates [73] to get the effective elastic properties of the mixture.

The Voigt estimate is given by:

$$E_V = E_{SS}v_{SS} + E_{IN}v_{IN} \text{ … (Eq. 5.2)}$$

The Reuss estimates are given by:

$$E_R = \frac{v_{SS}}{E_{SS}} + \frac{v_{IN}}{E_{IN}} \text{ … (Eq. 5.3)}$$

The Voigt-Reuss-Hill estimates are given by:

$$E_c = E_{VRH} = \frac{E_V + E_R}{2} \text{ … (Eq. 5.4)}$$

where $E_c$is the effective property of the mixture. The effective Poisson's ratio is given by:

$$\nu_c = \nu_{SS}v_{SS} + \nu_{IN}v_{IN} \text{ … (Eq. 5.5)}$$

The theoretical Young's modulus and Poisson's ratio listed in Table 5.2 were used in Eq. 5.4 and Eq. 5.5 to get the effective modulus and Poisson's ratio. We had used the measured density of the 100% samples to get the volume fractions. Finally, the effective modulus and Poisson's ratio can be used to determine the longitudinal and shear velocities:

$$C_{L_c} = \sqrt{\frac{E_c(1-\nu_c)}{\rho_c(1+\nu_c)(1-2\nu_c)}} \text{ … (Eq. 5.6)}$$

$$C_{T_c} = \sqrt{\frac{E_c}{2\rho_c(1+\nu_c)}} \text{ … (Eq. 5.7)}$$

Properties	**SS420**	**IN718**
Density (kg/m^3)	7880	8237
Young's Modulus (GPa)	224	195
Poisson's ratio	0.279	0.308

Table 5.2. Theoretical mechanical properties [74,75].

5.4. Results

5.4.1. Ultrasonic velocities

The longitudinal and shear wave velocities measured using the procedure described in Ch. 2.2.1 are shown in Fig. 5.2. The velocities were measured along all three directions, with D3 being the build direction. The shear measurements were also carried out in each direction with two polarizations. This will give a total of three pure modes per direction, which will allow us to measure anisotropy. Overlaying the RoM results with experimental data, we can observe that the DED velocities are lower than the literature values in certain directions.

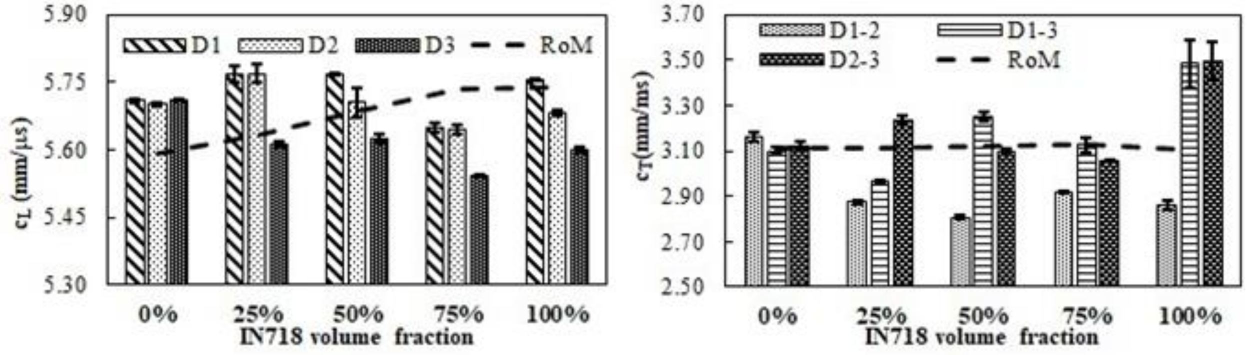

(a) (b)

Figure 5.2. (a) Longitudinal velocity along three directions, (b) Shear wave velocity along different shearing planes (Di−j), i is the propagation direction and j is the shear direction. RoM corresponds to the rule of mixture assuming the sample to be isotropic.

Between the three directions, we can also observe anisotropy, which is prominent in all the mixtures: 25%, 50%, 75%. While the RoM predicts a slightly increasing trend from 0% to 100%, we observe that the fractional mixtures have higher velocities compared to the pure samples. All the mixed fraction samples exhibit lower velocities along the build direction. This trend is consistent for the shear velocities as well, where the transverse plane to build direction, i.e., D1-2, has lower values compared to other directions for the mixed fractions. Interestingly, the shear properties of 100% IN718 was greater than the other fractions. The RoM predicts no change in shear velocity, however, we observe a considerable difference in velocity between the pure SS420 and IN718 samples, and the mixture samples.

5.4.2. Attenuation coefficient

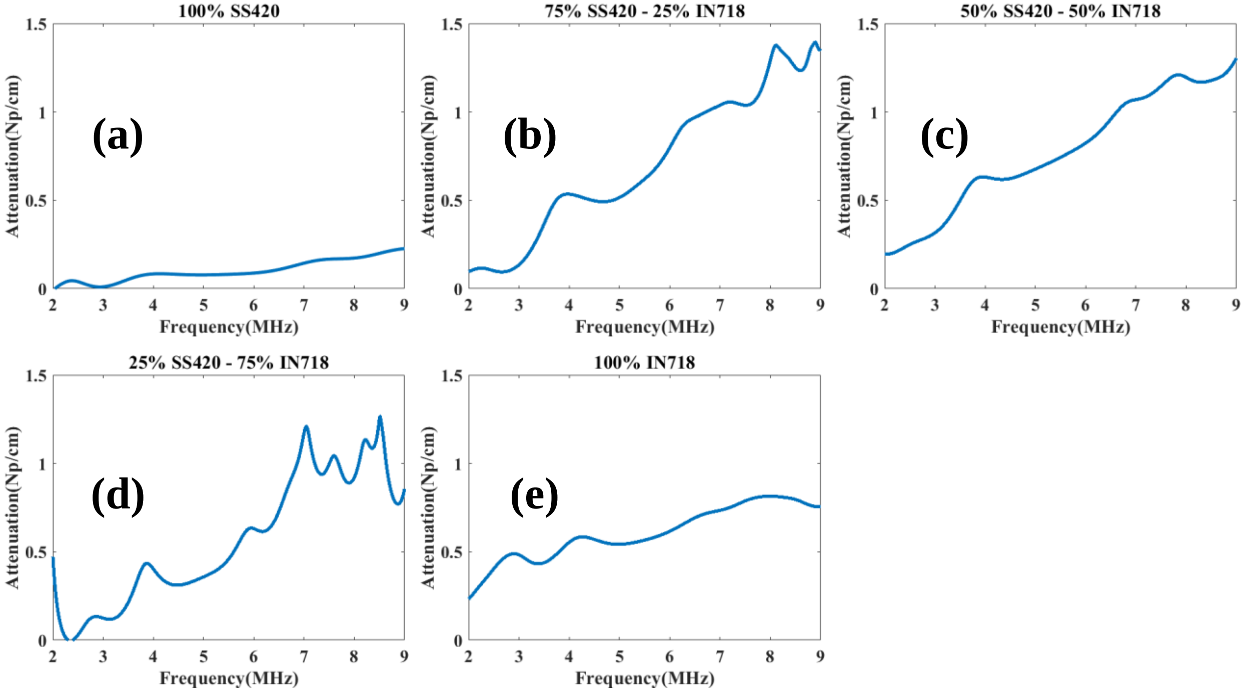

Figure 5.3. Attenuation coefficient as a function of frequency for (a) 100% SS420, (b) 25% IN718, (c) 50% IN718, (d) 75% IN718 and (e) 100% IN718.

From the velocity measurements, we could notice that the build direction has a significant influence on the measurements. Therefore, we chose to measure the attenuation coefficient only along the build direction for comparison. Fig. 5.3 shows the attenuation coefficient as a function of frequency calculated using Eq. 2.7 as described in Ch. 2.2.2. Since we use a 5 MHz transducer, we limit the frequency bandwidth to 2 – 9 MHz. From Fig. 5.3 we can notice that the pure SS420 has a lower attenuation coefficient compared to rest of the samples. The mixed fractions seem to have higher attenuation coefficient compared to the pure samples. The 25% and 50% IN718 samples exhibit the highest attenuation followed by the 75% and pure IN718 samples, which have nominally similar attenuation characteristics. We can observe “humps” or peaks in the attenuation curves, which will be discussed in Ch. 5.5.2. As a general observation, we can note that the mixed fractions and pure IN718 have strong peaks compared to SS420. Most of these peaks also appear to occur at 4, 7 and 8 MHz.

5.4.3. Backscatter coefficient

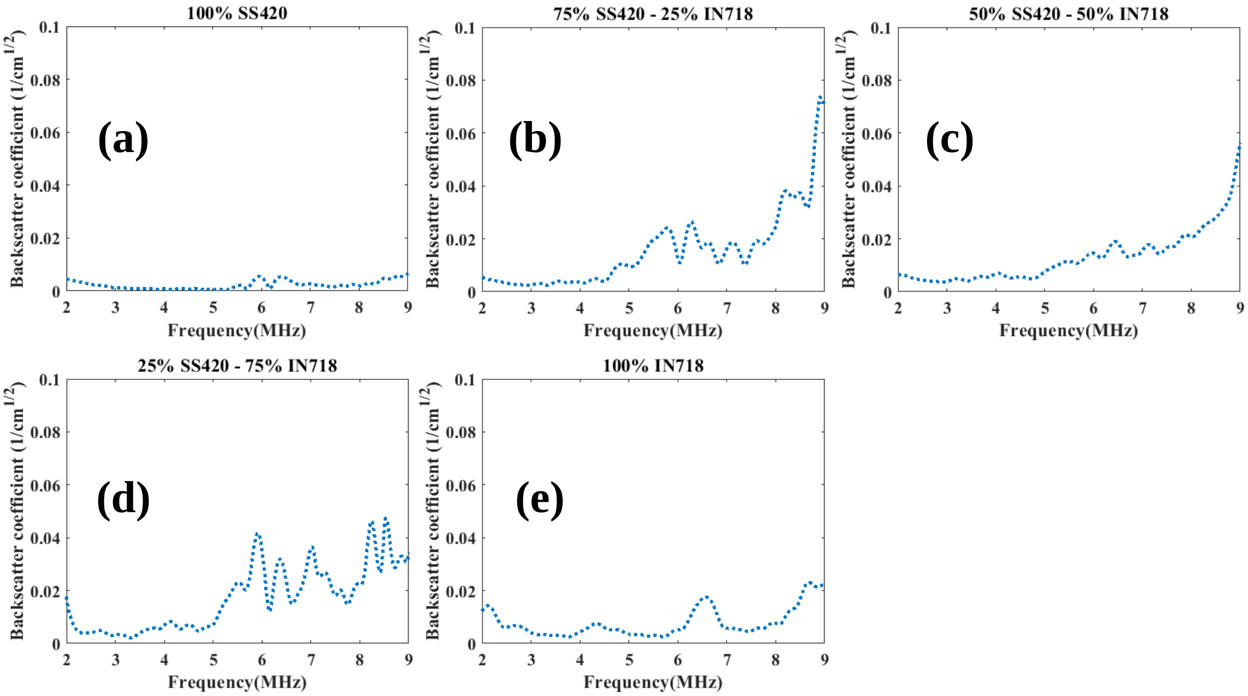

Figure 5.4. Backscatter coefficient as a function of frequency for (a) 100% SS420, (b) 25% IN718, (c) 50% IN718, (d) 75% IN718 and (e) 100% IN718.

The backscatter coefficient was calculated using Eq. 2.8 and as described in Ch. 5.2.3. Fig. 5.4 shows the backscatter coefficient for all the samples plotted as a function of frequency. Since this uses the absolute α measured from Fig. 5.3, we match the bandwidth of the backscatter coefficient to that of α. Typically, η has an increasing trend with frequency, which is consistent with Fig. 5.4. However, most η curves reported in the literature for IN718 [30,65] show a smooth behavior around the central frequency. In the present case, the mixed fractions show a sharp increase at 5 – 6 MHz. We noticed strong backscatter amplitude from the samples as shown in Fig. 5.1, which shows a A-Scan of the 100% SS420 sample and 25% IN718 samples. The backscatter region chosen for analysis is also shown. The 25% IN718 sample has considerably higher backscattered amplitude relative to the backwall. The strong grain noise may give rise to discrete peaks in the frequency domain as opposed to a smooth curve. Calculating η further gives rise to noise/ripples in the frequency domain due to these strong backscatter signals. Interestingly, the backscatter is highest for the cases where IN718 fraction is lower.

5.4.4. Elastic constants

C_{ij}	100% SS420	25% IN718	50% IN718	75% IN718	100% IN718
C_{11}	256.9 ± 0.4	264.4 ± 1.8	265.8 ± 0.2	257.8 ± 1.0	272.8 ± 0.3
C_{22}	256.1 ± 0.4	264.5 ± 1.8	258.5 ± 3.0	257.4 ± 1.0	266.0 ± 0.4
C_{33}	256.8 ± 0.2	250.3 ± 0.5	252.6 ± 0.9	248.0 ± 1.0	258.3 ± 0.3
C_{44}	76.9 ± 1.0	83.1 ± 1.0	76.8 ± 0.5	75.4 ± 0.3	100.6 ± 4.8
C_{55}	76.9 ± 1.0	70.0 ± 0.2	84.5 ± 1.0	78.9 ± 1.6	100.0 ± 5.9
C_{66}	76.9 ± 1.0	65.6 ± 0.2	63.0 ± 0.5	68.7 ± 0.3	67.3 ± 1.0
C_{11}^{t}	248	256	264	272	282
C_{66}^{t}	76.2	76.75	77.2	77.2	78.3

Table 5.3. Elastic constants measured from the ultrasonic velocities.

Using the ultrasonic velocities, we can determine the elastic constants of the structure. Typically, we assume these structures to be isotropic. However, the ultrasonic measurements allow us to measure any possible anisotropy that can result from the fabrication. Therefore, we start with the assumption that this could be quasi-isotropic, or orthotropic. Since we only have three pure modes per direction, we are limited by the number of elastic constants we can invert. Therefore, we will focus only on the leading diagonal of the stiffness matrix [62]. Using the pure modes, the elastic constants can be written as [15]: $C_{ij} = c_{ij}^2\rho$, where C_{ij} are the elastic constants, c_{ij} is the velocity and ρ is the density. For the pure mode cases, $i = j$, and $i, j = 1,2 \dots 6$. Values in Table 1 and Table 2 were used for the calculations. The results in Table 5.3 show the elastic constants values determined experimentally and the theoretically determined elastic constants using RoM equations, C_{11}^t and C_{66}^t. Since they are isotropic, we assume $C_{11}^t = C_{22}^t = C_{33}^t$ and $C_{44}^t = C_{55}^t = C_{66}^t$.

5.5. Discussions

Properties	100% SS420	25% IN718	50% IN718	75% IN718	100% IN718
Hardness (HV)	555 ± 18	207 ± 8	192 ± 5	235 ± 7	311 ± 9
UTS (MPa)	1926 ± 55	771 ± 61	697 ± 80	910 ± 33	1071 ± 57

Table 5.4. Mechanical properties of the sample [12].

To explain these observations, we use destructive characterization results provided by our collaborators [12]. The micrographs of all the samples in the build (vertical) direction are shown in Fig. 5.5. We can notice that the pure SS420 sample Fig. 5.5 (a), has elongated grains in the build direction, which points towards texture. However, rest of the samples shows strong dendritic grains (long slender grains), which coincides with the presence of IN718. Furthermore, macro-colonies of these dendritic grains can also be observed in the samples with IN718. To further understand the material composition at the microstructural scale, we analyze the X-Ray Diffraction (XRD) results shown in Fig. 5.6 where the presence of secondary and tertiary phases can be observed in the mixture and pure IN718 samples. The white outline along the grain boundaries in the mixture samples are meta-stable phases called Laves phases [12,26]; $(Ni,Fe,Cr)_2(Nb,Mo,Ti)$. Additionally, the tiny black spots found in the micrographs Fig. 5.5 (c, e), were initially thought to be voids, but a chemical analysis noted that they were carbide rich phases (Nb,Ti)C [12]. Hardness and ultimate tensile strength (UTS) were also measured by our collaborators and are shown in Table 5.4.

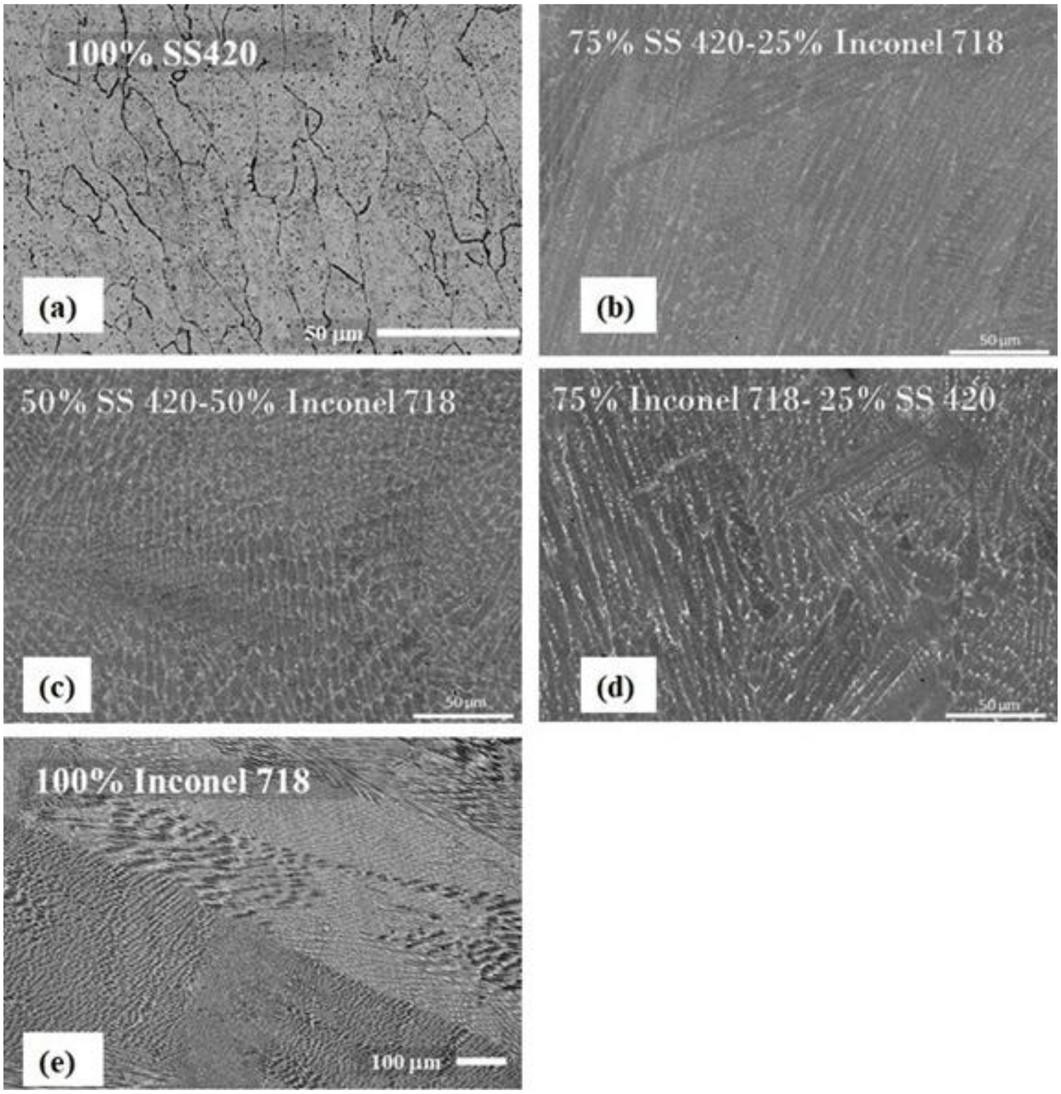

Figure 5.5. Micrographs of (a) 100% SS420, (b) 25% IN718, (c) 50% IN718, (d) 75% IN718 and (e) 100% IN718. The vertical direction is the build direction (z-axis). The images are sections of the XZ, YZ planes [12].

5.5.1. Elastic properties

We can observe that the C_{11} values of the mixture samples are lower than conventional samples. This can be partly attributed to the wide distribution of carbide phases, which are known to have a lower modulus [26,76]. The presence of texture can also result in anisotropic properties, which is also captured in the elastic constants. Interestingly, each composition shows a slightly different symmetry. Basing the arguments only on the leading diagonal of the stiffness matrix, we can see that the pure SS420 exhibits isotropic properties, $C_{11} \approx C_{22} \approx C_{33}$ and $C_{44} \approx C_{55} \approx C_{66}$. The micrograph shows elongated grains, and the shear properties in the build plane are slightly different.

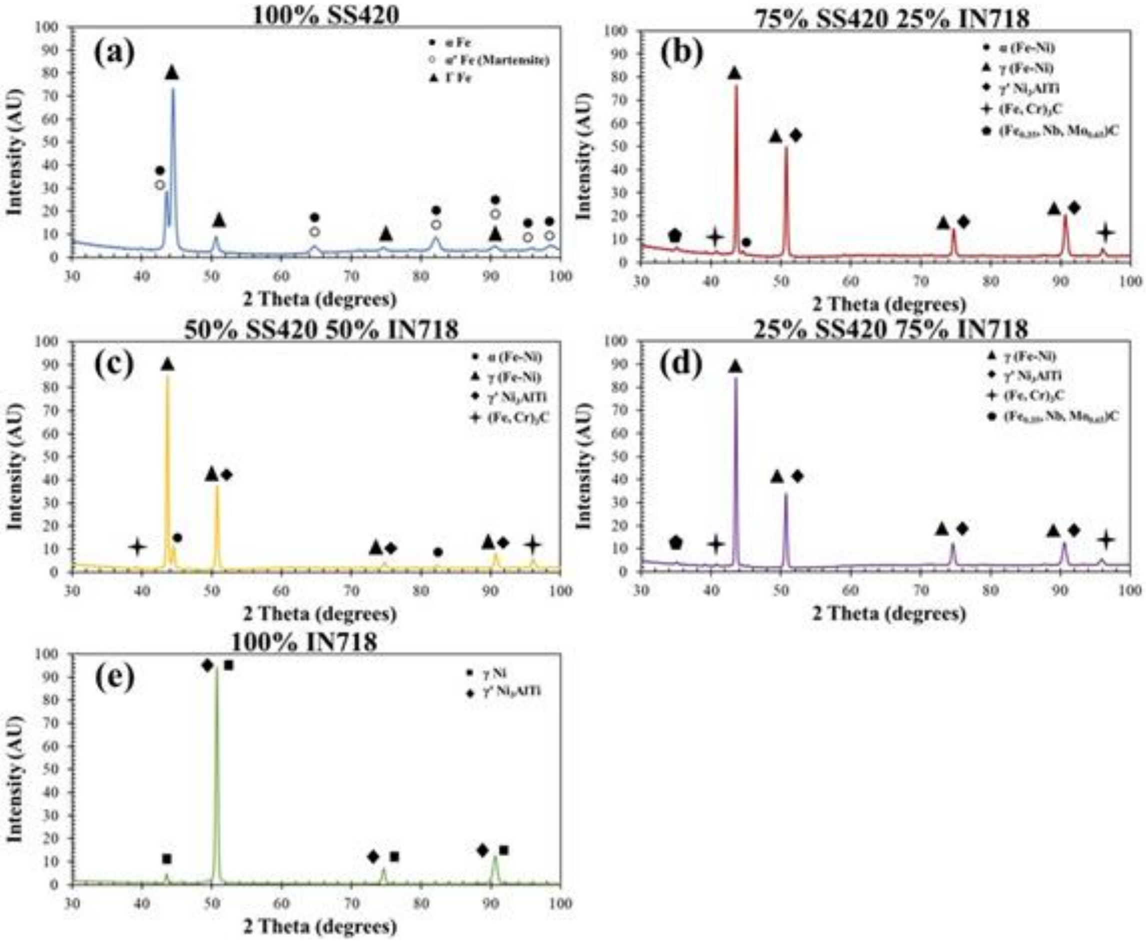

Figure 5.6. XRD analysis showing different phases for (a) 100% SS420, (b) 25% IN718, (c) 50% IN718, (d) 75% IN718 and (e) 100% IN718 [12].

The samples with IN718 exhibit a tetragonal or hexagonal symmetry. This is most prominent in 75% and 100% IN718. While rest of the elastic constants are needed to build a complete picture, we can infer from the limited results that the presence of IN718 changes the bulk anisotropy of the structure. This change can be partially attributed to the large amount of Laves phases, especially in the IN718 samples. Laves phase has a hexagonal symmetry [26], while γ'' is body-centered-tetragonal (bct) [26] and γ is face-centered-cubic (fcc) [26]. We notice from the XRD images in Fig. 5.6, that there may be very small amount of γ' and γ''. However, it is difficult to distinguish between the γ, γ' and γ'' phases via XRD analysis since all γ phase peaks typically overlap. The dissolution of γ'' is expected in DED samples, since the carbide and Laves phases tend to absorb the Nb rich sites, thus starving the sample of Nb, which is the primary component of γ''. In general, γ' and γ'' are gained through controlled heat treatment cycles, and they are less likely to be formed with rapid cooling in the DED process. The loss of γ' and γ'' strengthening mechanisms is also the reason for lower strength and hardness of samples with IN718. This is especially true for the fractional mixtures which have the lowest strength and hardness as shown in Table 5.4.

5.5.2. Attenuation coefficient

From the micrographs in Fig. 5.5, we can observe that there are large colonies of micro-grains. These colonies are much larger than the usual grains observed in conventional fabrication processes, with some colonies approaching 500 microns. This structure can be observed only in the presence of IN718. Therefore, it is expected that the attenuation of pure SS420 will be the lowest compared to any mixture with IN718. The attenuation results in Fig. 5.3 confirms this hypothesis. Moving to the fractions, it is interesting to note that the highest attenuation coefficient is exhibited by the sample with the 25% IN718, which is contrary to the earlier observation. From the hardness and UTS measurements, we can notice that 25% also has the lowest numbers. Based on the earlier argument of lower γ'', and higher carbide phases, we can conjecture that the volume fraction of the Laves and carbide phase might be higher in the fractional mixtures. Niobium and

Molybdenum are refractory alloys which have high thermoelastic attenuation [77]. Since the Laves phases have large amount of these alloys, we can conjecture that the attenuation can also be higher. This argument agrees well with the experimental observations. Furthermore, we can observe "humps or peaks" at certain frequencies in all the attenuation coefficient vs frequency plots. These have been traditionally characterized as peaks arising from Rayleigh to stochastic transition due to macro and micrograins in duplex microstructures [46,64]. The transition occurs at $k\overline{d} = 1$, where k is wavenumber and $\overline{d}$ is the average grain size. The challenge with applying these theories to DED structures such as Fig. 5.5 is the definition of grain size. In IN718, due to the strong presence of Laves phase, we get cellular structures. If we assume the grain size to the same as the cell size, the needle like geometry makes it challenging to do any analysis. Furthermore, we expect to get peaks or transition in the 200 MHz range based on the cell size (≈ 5 – 10 μm). However, a collection/cluster of the cells, also called as macrograins, seem like a more plausible source of scattering. The approximate cluster size (≈ 100 – 500 μm) can give peaks at the lower frequencies (< 10 MHz) which is what we observe in Fig. 5.3. The influence of microstructure on the apparent position of the peaks will be explored elsewhere.

5.5.3. Backscatter coefficient

The general conception of attenuation and backscatter is that a sample with higher attenuation will also have higher backscatter. This comes from the idea that the ultrasonic wave is scattered back as it propagates forward and therefore smaller amount of energy gets reflected from the backwall, which is ultimately used to calculate the attenuation coefficient. This idea bodes well for the current results with the 25% IN728 sample once again demonstrating the highest backscatter coefficient as shown in Fig. 5.4 (b). We find "peaks" at specific frequencies in the backscatter coefficient as a function of frequency. These peaks are once again observed when the $k\overline{d} = 1$. Since a uniform grain distribution cannot be observed, we expect large back scatter amplitudes when the wave interacts with a single large grain. This will give rise to distinct echoes at frequencies or $k\overline{d}$ which match the specific grain size. This is consistent between experimental results and the micrographs shown in Fig. 5.5. An interesting observation can be made regarding the scattering phenomenon by using the anisotropy index. Since both Fe and Ni are cubic systems, we can use the Zener anisotropy index: $2\, C_{44}/(C_{11} - C_{12})$. Using single crystal properties for Fe and Ni [77], we can get the Zener index as: Fe (2.4) and Ni (1.23). This suggests that the SS component of the mixtures will have a higher scattering coefficient compared to the Ni. However, the results suggest that the even 25% of IN718 in the mixture will contribute to higher scattering compared to SS420. We can conjecture that the larger cluster size of IN718 will result in higher attenuation and backscatter despite the Zener index being half of that of SS420. IN718 also has γ'' which is bct [26], and Laves phase which is hexagonal [26], both of which can contribute to higher anisotropy and additional scattering and absorption. Further explorations are necessary to completely understand the results.

5.5.4. Rule of mixture

The velocity and elastic constants suggest that the simple rule of mixtures may not apply for the DED mixture samples. The destructive tests and ultrasonic results suggest that the formation of meta-stable phases and carbide inclusions could be the main reason behind the violation of RoM. The volume fraction of these secondary phases as a function of different mixture fractions remains to be explored. The reason for the higher or lower volume fraction of secondary phases also remains an open question. The rationale behind using the RoM was primarily to compare the elastic properties. While, RoM has been used extensively for anisotropic structures like composites [78], the simple formulation used here was not expected to capture the effects since the grains are not equiaxed and uniform. Other forms of RoM such as the mean field homogenization or the Mori-Tanaka method might be able to capture the effects but are beyond the scope of this work. It is interesting to note that the measured experimental density does not follow the RoM either. We are presenting a novel in-situ fabrication method, which allows us to mix different metallic structures while fabricating the bulk structure. This provides us with a high degree of flexibility in fabrication compared to techniques like powder metallurgy, however, we lose the accuracy of weight fractions. The weight fraction values we use for comparison are theoretical and may not be the exact values. We humbly recognize this with the reservation that there is no other method to measure the exact weight of each material in the crystallized state.

5.5.5. Heterogeneity

From the backscatter coefficient measurements, we observed that all the samples exhibit considerable spatial heterogeneity of ultrasonic properties. An example C-Scan of the 25% IN718 sample is shown in Fig. 5.7. While the scan area is only 10 mm X 10 mm, we notice a 27% difference in backwall amplitude. Similarly, the RMS backscatter value varies by as much as 68%. A backscatter RMS C-Scan was obtained by taking the root mean square of backscatter amplitude; $\Gamma(\omega)$ in the frequency domain (2 – 9 MHz) at every single point in the C-Scan [65]. This will give us a single value (Backscatter RMS) at every spatial point, which can be further plotted as a 2D image as shown in Fig. 5.7 (b). The backscatter RMS also shows localized areas where the backscatter value is large. The heterogeneous distributions highlight the complexity of characterizing and utilizing specific DED structures. This further raises questions such as the validity of the backscatter and attenuation measurements similar to what was raised by Dr. Panetta

[64]. The inhomogeneity can cause significant phase aberrations within the beam as the ultrasonic beam propagates, which will make the attenuation and backscatter coefficients become functions of the interaction volume.

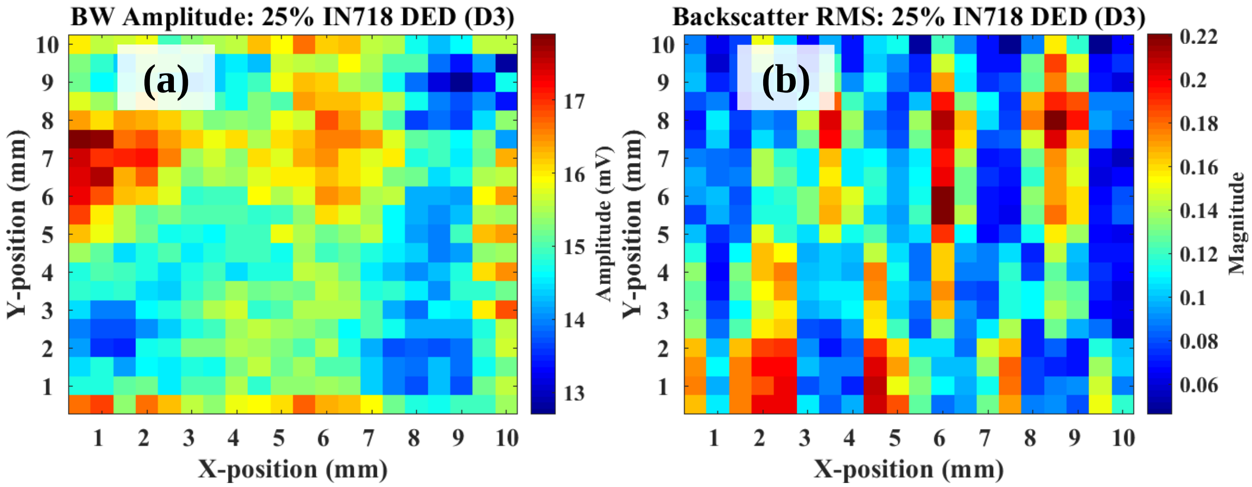

Figure 5.7. Spatial C-Scan of the 25% IN718 sample for (a) backwall amplitude (BW), (b) Backscatter RMS calculated in the frequency domain.

5.6. Conclusions

The present chapter explores the use of ultrasonics to characterize multi-material structures fabricated using in-situ DED method. The main focus of the chapter was to use the same techniques to compare between the different mixtures. The ultrasonic parameters including velocity, attenuation and backscatter coefficient show some degree of anisotropy. The elastic constants calculated from the velocities also point towards varied anisotropy properties based on the mixture fraction. The theoretical velocities and elastic constants calculated using a simple rule of mixture were not consistent with the experimentally measured values. The samples with mixtures also showed higher degree of spatially varying properties including ultrasonic attenuation and backscatter. The anomalous behavior of ultrasonic properties of the mixtures can be narrowed down to the presence of IN718. The resulting microstructure from its presence seems to change the crystallization of the bulk structure, resulting in complex secondary phases. These results suggest that a larger study of just DED fabricated IN718 is warranted. Similarly, mixture of other structures needs to be studied carefully to fully understand the limits of performance of the multi-material structures. We believe understanding the ultrasonic characteristics will eventually help us to understand solidification dynamics using nondestructive means.

CHAPTER 6. CONCLUSIONS AND FUTURE WORK

The main purpose of this work was to develop nondestructive qualification strategies for laser-AM nickel-based superalloys using ultrasonic testing as the characterization tool. It was demonstrated that ultrasonic velocities, attenuation coefficient, and backscatter coefficient can be used for the characterization of these complex materials given their sensitivity to the microstructural features of laser-DED samples. These results were compared to the ultrasonic response of a conventional hot-rolled IN718 sample in Ch. 3 where a significant degree of anisotropy was observed in the laser-DED sample, moreover, the laser-DED attenuation and backscatter coefficients vs frequency plots showed the presence of the interaction peaks at different frequencies, especially around 5 MHz; these peaks represent a Rayleigh to stochastic scattering mechanism transition that occur when the length of the ultrasonic wave matches the macrograin size.

Furthermore, the usefulness of the aforementioned ultrasonic parameters was demonstrated with the proposed qualification parameters to quantify anisotropy, heterogeneity or grain size in Ch. 4 that were derived using the ultrasonic velocities, attenuation coefficients and back-wall amplitude C-Scans. These parameters captured the differences between two IN718 laser-DED samples fabricated with slightly different processing parameters.

Finally, the ultrasonic response of multi-material structures varying from 100% SS420 to 100% IN718 by 25 wt% were measured. The ultrasonic velocities measured experimentally were not consistent with a rule of mixture calculation using theoretical results. Furthermore, the attenuation coefficient of the samples with IN718 content showed similar peaks as presented in Ch. 3, and these results do not follow a linear trend. This reinforces the idea that predictability of mechanical properties is not guaranteed and that a qualification procedure that takes into account the complexity of laser-AM nickel superalloys is needed.

As future work, a study of the ultrasonic response of laser-DED IN718 samples fabricated with different processing parameters and at specific steps from a standard heat treatment procedure will be performed. The objective is to track the microstructural evolution with the qualification parameters proposed in this work; the reasoning is that after the heat treatment, the samples will have an ultrasonic response similar to the hot-rolled sample. Eventually, this study will be extended to include IN718 samples fabricated with other fabrication methods.

REFERENCES

REFERENCES

[1] Lucas W. Koester, Leonard J. Bond, Peter C. Collins, Hossein Taheri. “Additive Manufacturing for the Aerospace Industry”, Ch. 18. 401–417, 2019. https://doi.org/10.1016/B978-0-12-814062-8.00020-0

[2] Bhaskar Dutta, Sudarsanam Babu and Bradley Jared, 2019. “Science, Technology and Applications of Metals in Additive Manufacturing”. Ch. 8. https://doi.org/10.1016/C2017-0-04707-9

[3] Michael Gorelik. “Additive manufacturing in the context of structural integrity”. International Journal of Fatigue 94 (2017) 168–177. https://doi.org/10.1016/j.ijfatigue.2016.07.005

[4] L. Koester, H. Taheri, L. J. Bond, D. Barnard, and J. Gray. “Additive Manufacturing Metrology: State of the Art and Needs Assessment”. AIP Conference Proceedings 1706, 130001 (2016); https://doi.org/10.1063/1.4940604

[5] J. A. Slotwinski. “Additive manufacturing: Overview and NDE challenges”. AIP Conference Proceedings 1581, 1173 (2014); https://doi.org/10.1063/1.4864953

[6] Q. Y. Lu & C. H. Wong (2018) “Additive manufacturing process monitoring and control by non-destructive testing techniques: challenges and in-process monitoring”, Virtual and Physical Prototyping, 13:2, 39–48, DOI: 10.1080/17452759.2017.1351201

[7] Q. Y. Lu & C. H. Wong (2017) “Applications of non-destructive testing techniques for post-process control of additively manufactured parts, Virtual and Physical Prototyping”, 12:4, 301–321, DOI: 10.1080/17452759.2017.1357319

[8] Matthias Hirsch, Rikesh Patel, Wenqi Li, Guangying Guan, Richard K. Leach. Steve D. Sharples, Adam T. Clare. “Assessing the capability of in-situ nondestructive analysis during layer based additive manufacture”. Additive Manufacturing 13 (2017) 135–142. https://doi.org/10.1016/j.addma.2016.10.004

[9] Volker Carl. “Monitoring system for the quality assessment in additive manufacturing”. AIP Conference Proceedings 1650, 171 (2015); https://doi.org/10.1063/1.4914607

[10] Mohsen Seifi, Michael Gorelik, Jess Waller, Nik Hrabe, Nima Shamsaei, Steve Daniewicz, and John J. Lewandowski. “Progress Towards Metal Additive Manufacturing Standardization to Support Qualification and Certification”. JOM, Vol. 69, No. 3, 2017. DOI: 10.1007/s11837-017-2265-2

[11] Babu, S.S., Raghavan, N., Raplee, J. et al. “Additive Manufacturing of Nickel Superalloys: Opportunities for Innovation and Challenges Related to Qualification”.

Metall Mater Trans A 49, 3764–3780 (2018). https://doi.org/10.1007/s11661-018-4702-4

[12] B. Aydogan, A. O’Neil, and H. Sahasrabudhe, “Microstructural and mechanical characterization of stainless steel 420 and Inconel 718 multi-material structures fabricated using 425 laser directed energy deposition," Journal of Manufacturing Processes 68 (2021) 1224–1235. https://doi.org/10.1016/j.jmapro.2021.06.031

[13] Zhao X, Chen J, Lin X, Huang W. “Study on microstructure and mechanical properties of laser rapid forming Inconel 718”, Materials Science and Engineering A 478 (2008) 119–124. https://doi:10.1016/j.msea.2007.05.079

[14] Hosseini E, Popovich VA. “A review of mechanical properties of additively manufactured Inconel 718”. Additive Manufacturing 30 (2019) 100877. https://doi.org/10.1016/j.addma.2019.100877

[15] Parimi L, Ravi GA, Clark D, Attalah M. “Microstructural and texture development in direct laser fabricated IN718”, Materials Characterization 89 (2014) 102–111. http://dx.doi.org/10.1016/j.matchar.2013.12.012

[16] Holland S, Wang X, Fang XY, Guo YB, Yan F, Li L. “Grain boundary network evolution in Inconel 718 from selective laser melting to heat treatment”. Materials Science & Engineering A 725 (2018) 406–418. https://doi.org/10.1016/j.msea.2018.04.045

[17] Rezaei A, Rezaeian A, Kermanpur A. “Microstructural and mechanical anisotropy of selective laser melted IN718 superalloy at room and high temperatures using small punch test”. Materials Characterization 162 (2020) 110200. https://doi.org/10.1016/j.matchar.2020.110200

[18] Ni M, Chen C, Wang X, Wang P, Li R, Zhang Z, Zhou K. “Anisotropic tensile behavior of in situ precipitation strengthened Inconel 718 fabricated by additive manufacturing”. Materials Science & Engineering A 701 (2017) 344–351. http://dx.doi.org/10.1016/j.msea.2017.06.098

[19] Du D, Dong A, Shu D. “Influence of build orientation on microstructure, mechanical and corrosion behavior of Inconel 718 processed by selective laser melting”. Materials Science & Engineering A 760 (2019) 469–480. https://doi.org/10.1016/j.msea.2019.05.013

[20] Li Z, Chen J, Sui S. “The microstructure evolution and tensile properties of Inconel 718 fabricated by high-deposition-rate laser directed energy deposition”. Additive Manufacturing 31 (2020) 100941. https://doi.org/10.1016/j.addma.2019.100941

[21] V. K. Nadimpalli. “Ultrasonic nondestructive evaluation of metal additive manufacturing,” Ph.D. thesis, University of Louisville, 2018.

[22] F. Honarvar and A. Varvani-Farahani, “A review of ultrasonic testing applications in additive manufacturing: Defect evaluation, material characterization, and process control," Ultrasonics 106227 (2020)

[23] Khabouchi A, Ventura P. “Crystallographic texture and velocities of ultrasonic waves in a Ni-based superalloy manufactured by laser powder bed fusion”. Materials Characterization 169 (2020) 110607. https://doi.org/10.1016/j.matchar.2020.110607

[24] Mei Y, Liu Y, Liu C. “Effects of hot rolling on the precipitation kinetics and the morphology evolution of intermediate phases in Inconel 718 alloy”. Journal of Alloys and Compounds 649 (2015) 949–960. http://dx.doi.org/10.1016/j.jallcom.2015.07.149

[25] “Attenuation of ultrasonic waves in rolled metals”. J. Acoust. Soc. Am. 116 (6), December 2004. https://doi.org/10.1121/1.1810236

[26] D. Deng, “Additively manufactured Inconel 718: Microstructures and mechanical properties," Ph.D. thesis, Linkoping University, 2018.

[27] P. H. Rogers and A. L. Van Buren, “An exact expression for the Lommel-diffraction correction integral," the Journal of the Acoustical Society of America 55(4), 724–728 (1974).

[28] L.W. Schmerr, “Fundamentals of Ultrasonic Nondestructive Evaluation: A Modeling Approach,”. 2nd Edition. Springer, Switzerland, 2016

[29] F. J. Margetan, R. B. Thompson, I. Yalda-Mooshabad, and Y. K. Han, “Detectability of Small Flaws in Advanced Engine Alloys,” U.S. Air Force Technical Report, Center for NDE, Iowa State University, Ames, Iowa (1993).

[30] P. D. Panetta, H. Du, and W. Hassan, “Grain size measurements using ultrasonic backscattering," Review of Progress in Quantitative Nondestructive Evaluation (2019).

[31] Mostafa A, Picazo Rubio I, Brailovski V, Jahazi M, Medraj M. Structure, Texture and Phases in 3D Printed IN718 Alloy Subjected to Homogenization and HIP Treatments. Metals. 2017; 7(6):196. https://doi.org/10.3390/met7060196

[32] Ni M, Liu S, Chen C, Li R, Zhang X, Zhou K. “Effect of heat treatment on the microstructural evolution of a precipitation-hardened superalloy produced by selective laser melting”, Materials Science & Engineering A 748 (2019) 275–285. https://doi.org/10.1016/j.msea.2019.01.109

[33] Zhang X, McMurtrey M, Wang L. “Evolution of Microstructure, Residual Stress, and Tensile Properties of Additively Manufactured Stainless Steel Under Heat Treatments”. JOM, Vol. 72, No. 12, 2020. https://doi.org/10.1007/s11837-020-04433-9

[34] Silva C, Song M, Leonard K, Wang M, Was G, Busby J. “Characterization of alloy 718 subjected to different thermomechanical treatments”. Materials Science & Engineering A 691 (2017) 195–202. http://dx.doi.org/10.1016/j.msea.2017.03.045

[35] Qi, H., Azer, M. & Ritter, A. Studies of Standard Heat Treatment Effects on Microstructure and Mechanical Properties of Laser Net Shape Manufactured INCONEL 718. Metall Mater Trans A 40, 2410–2422 (2009). https://doi.org/10.1007/s11661-009-9949-3

[36] B.A. Cowles, Summary Report: The Second Joint Federal Aviation Administration—Air Force Workshop on Qualification/Certification of Additively Manufactured Parts, Dayton, OH, 2017

[37] M.A. Dvorack, T.J. Kerschen, E.W. Collins, Product Acceptance Environmental and Destructive Testing for Reliability, SAND2007-5171, Sandia National Laboratories, Albuquerque, NM, 2007

[38] Chang-Jun Bae, Alisha B. Diggs, Arathi Ramachandran. “Additive Manufacturing: Materials, Processes, Quantifications and Applications, Ch. 6 “Quantification and certification of additive manufacturing materials and processes”. 2018 Elsevier Inc. https://doi.org/10.1016/C2016-0-01595-4

[39] ASTM F3187-16 standard guide for DED of metals

[40] ASTM F3055-14a standard specification for AM nickel alloy (UNS N07718) with powder bed fusion

[41] ASTM F3056-14 standard specification for AM nickel alloy ((UNS N06625) with powder bed fusion

[42] ASTM F3122-14 standard guide for evaluating the mechanical properties of metal materials made via AM processes

[43] ASTM E3166-20 standard guide for nondestructive examination of metal additively manufactured aerospace parts after build

[44] Ledbetter H and Migliori A, “A general elastic-anisotropy measure”, Journal of Applied Physics 100, 063516 (2006); https://doi.org/10.1063/1.2338835

[45] Ze Chen, Changjun Han, Ming Gao, Sastry Yagnanna Kandukuri & Kun Zhou (2022) A review on qualification and certification for metal additive manufacturing, Virtual and Physical Prototyping, 17:2, 382–405, DOI: 10.1080/17452759.2021.2018938

[46] F. E. Stanke, G. S. Kino, A unified theory for elastic wave propagation in polycrystalline materials, The Journal of the Acoustical Society of America 573 75 (3) (1984) 665–681.

[47] Arguelles A, Turner J, "Ultrasonic attenuation of polycrystalline materials with a distribution of grain size", The Journal of the Acoustical Society of America 141, 4347 (2017); doi: 10.1121/1.4984290

[48] Ono K, "A Comprehensive Report on Ultrasonic Attenuation of Engineering Materials, Including Metals, Ceramics, Polymers, Fiber-Reinforced Composites, Wood, and Rocks", Appl. Sci. 2020, 10(7), 2230; https://doi.org/10.3390/app10072230

[49] Shivakumar I. Ranganathan and Martin Ostoja-Starzewski, "Universal Elastic Anisotropy Index", Phys. Rev. Lett. 101, 055504 – Published 1 August 2008

[50] M. Askari, D. A. Hutchins, P. J. Thomas, L. Astolfi, R. L. Watson, M. Abdi, M. Ricci, S. Laureti, L. Nie, S. Freear, et al., Additive manufacturing of metamaterials: A review, Additive Manufacturing (2020) 101562.

[51] X. Wu, Y. Su, J. Shi, Perspective of additive manufacturing for metamaterials development, Smart Materials and Structures 28 (9) (2019) 093001.

[52] W. E. Frazier, Metal additive manufacturing: a review, Journal of Materials Engineering and performance 23 (6) (2014) 1917–1928.

[53] J. J. Lewandowski, M. Seifi, Metal additive manufacturing: a review of mechanical properties, Annual review of materials research 46 (2016) 151–186.

[54] B. Nagesha, V. Dhinakaran, M. V. Shree, K. M. Kumar, D. Chalawadi, T. Sathish, Review on characterization and impacts of the lattice structure 487 in additive manufacturing, Materials Today: Proceedings 21 (2020) 916–919.

[55] A. Bandyopadhyay, B. Heer, Additive manufacturing of multi-material structures, Materials Science and Engineering: R: Reports 129 (2018) 1–16.

[56] J. Kennedy, L. Flanagan, L. Dowling, G. Bennett, H. Rice, D. Trimble, The influence of additive manufacturing processes on the performance of a periodic acoustic metamaterial, International Journal of Polymer Science 2019 (2019).

[57] B. Onuike, B. Heer, A. Bandyopadhyay, Additive manufacturing of inconel 718—copper alloy bimetallic structure using laser engineered net shaping (lens™), Additive Manufacturing 21 (2018) 133–140.

[58] H. Sahasrabudhe, R. Harrison, C. Carpenter, A. Bandyopadhyay, Stainless steel to titanium bimetallic structure using lens™, Additive Manufacturing (2015) 1–8.

[59] D. Wu, X. Liang, Q. Li, L. Jiang, Laser rapid manufacturing of stainless steel 316l/inconel718 functionally graded materials: microstructure evolution and mechanical properties, International Journal of Optics 2010 (2010).

[60] C. Toh, Design, evaluation and optimisation of cutter path strategies when high speed machining hardened mould and die materials, Materials & de510 sign 26 (6) (2005) 517–533.

[61] B. E. Carroll, R. A. Otis, J. P. Borgonia, J.-o. Suh, R. P. Dillon, A. A. Shapiro, D. C. Hofmann, Z.-K. Liu, A. M. Beese, “Functionally graded material of 304L stainless steel and Inconel 625 fabricated by directed energy deposition: Characterization and thermodynamic modeling”, Acta Materialia 108 (2016) 46–54.

[62] M. Musgrave, Crystal acoustics, Acoustical Society of America New York, 2003.

[63] A. B. Bhatia, Ultrasonic absorption: an introduction to the theory of sound absorption and dispersion in gases, liquids, and solids, Courier Corporation, 1985.

[64] P. D. Panetta, Backscattering and attenuation during the propagation of ultrasonic waves in duplex titanium alloys, Ph.D. thesis, Iowa State University (1999).

[65] P. D. Panetta, L. G. Bland, M. Tracy, W. Hassan, Ultrasonic backscattering measurements of grain size in metal alloys, in: TMS 2014: 143rd Annual Meeting & Exhibition, Springer, 2014, pp. 723–730.

[66] P. Panetta, F. J. Margetan, I. Yalda, R. B. Thompson, Ultrasonic attenuation measurements in jet-engine titanium alloys, in: Review of Progress in Quantitative Nondestructive Evaluation, Springer, 1996, pp. 1525–1532.

[67] R. B. Thompson, F. Margetan, P. Haldipur, L. Yu, A. Li, P. Panetta, H. Wasan, Scattering of elastic waves in simple and complex polycrystals, Wave Motion 45 (5) (2008) 655–674.

[68] C. Kim, H. Yin, A. Shmatok, B. C. Prorok, X. Lou, K. H. Matlack, Ultrasonic nondestructive evaluation of laser powder bed fusion 316l stainless steel, Additive Manufacturing 38 (2021) 101800.

[69] L. Koester, R. A. Roberts, D. J. Barnard, S. Chakrapani, S. Singh, R. Hogan, L. J. Bond, Nde of additively manufactured components with embedded defects (reference standards) using conventional and advanced ultrasonic methods, in: AIP Conference Proceedings, Vol. 1806, AIP Publishing LLC, 2017, p. 140006.

[70] G. Huanes-Alvan, A. O’Neil, H. Sahasrabudhe, S. Chakrapani, Baseline estimation of ultrasonic response of metallic structures fabricated via laser direct energy deposition (DED), Review of Progress in Quantitative Nondestructive Evaluation (2019).

[71] F. J. Margetan, R. B. Thompson, I. Yalda-Mooshabad, Y. K. Han, Detectability of small flaws in advanced engine alloys (1993).

[72] P. H. Rogers, A. L. Van Buren, An exact expression for the Lommel-diffraction correction integral, the Journal of the Acoustical Society of America 55 (4) (1974) 724–728.

[73] R. Hill, Elastic properties of reinforced solids: some theoretical principles, Journal of the Mechanics and Physics of Solids 11 (5) (1963) 357–372.

[74] Stainless steel - grade 420 (uns s42000)-datasheet, https://www.azom.com/article.aspx?ArticleID=972, accessed: 04/23/2021.

[75] Maher in718 alloy data sheet, https://www.maher.com/media/pdfs/559718-datasheet.pdf, accessed: 04/23/2021.

[76] Z. Baicheng, L. Xiaohua, B. Jiaming, G. Junfeng, W. Pan, S. Chen-nan, N. Muiling, Q. Guojun, W. Jun, Study of selective laser melting (slm) inconel 718 part surface improvement by electrochemical polishing, Materials & Design 116 (2017) 531–537.

[77] R. Truell, C. Elbaum, B. B. Chick, Ultrasonic methods in solid state physics, Academic press, 2013.

[78] V. V. Vasiliev, R. M. Jones, L. I. Man, Mechanics of composite structures, CRC Press, 2017.